

THESIS FOR THE DEGREE OF LICENTIATE OF
ENGINEERING

Dynamic local structural symmetries and luminescence
properties of the yellow emitting phosphor Ce^{3+} -doped
 $\text{Y}_3\text{Al}_5\text{O}_{12}$

Yuan-Chih Lin



CHALMERS

Department of Physics
CHALMERS UNIVERSITY OF TECHNOLOGY
Göteborg, Sweden 2016

**Dynamic local structural symmetries and luminescence properties
of the yellow emitting phosphor Ce³⁺-doped Y₃Al₅O₁₂**

Yuan-Chih Lin

©Yuan-Chih Lin, 2016.

Department of Physics
Chalmers University of Technology
SE-412 96 Göteborg, Sweden

Chalmers Reproservice
Göteborg, Sweden 2016

Dynamic local structural symmetries and luminescence
properties of the yellow emitting phosphor Ce^{3+} -doped
 $\text{Y}_3\text{Al}_5\text{O}_{12}$

Yuan-Chih Lin
Department of Physics
Chalmers University of Technology

Abstract

This thesis centers on investigations of the local structure and vibrational properties of the oxide garnet $\text{Y}_3\text{Al}_5\text{O}_{12}$ (YAG), which when substituted with a few percent of the activator ion Ce^{3+} to replace Y^{3+} ($\text{Y}_{3-x}\text{Ce}_x\text{Al}_5\text{O}_{12}$, $\text{YAG}:\text{Ce}^{3+}$) is one of the most important phosphors for solid state lighting. The study builds on a comprehensive analysis of the nature of the phonons and localized vibrational modes in $\text{YAG}:\text{Ce}^{3+}$ and how these depend on the Ce^{3+} concentration and temperature and how they affect key optical properties, such as the intensity and frequency of the emitted light. The investigations have been carried out by using a combination of Raman, infrared, luminescence, and neutron spectroscopies, together with mode-selective vibrational excitation, and are further supported by computer modeling. The results show that the static and dynamic structure of $\text{YAG}:\text{Ce}^{3+}$ are dependent on both Ce^{3+} concentration and temperature. The substitution of the heavier Ce^{3+} ions compared to Y^{3+} is found to lower the vibrational frequencies of most of the phonons and localized vibrational modes around the Ce^{3+} ions, implying that they become more populated at a given temperature. As the temperature increases, vibrational modes of higher and higher frequency are activated, some of which induce significant dynamical tetragonal distortions around the Ce^{3+} ions. These distortions are shown to lead to a red-shift of the frequency of the emitted light. In addition, some of the high-frequency phonons are shown to be notably related to non-radiative relaxation of the excited-state electrons of the Ce^{3+} ions *via* electron-phonon coupling, which decreases the emission intensity when these phonons are activated. The reduction in emission intensity at elevated temperature is however a complicated process as it is found to relate also to thermal ionization of the excited-state electrons into the conduction band of the host crystal, which may be followed by charge trapping by defects.

Keywords: *phosphor, garnet, luminescence, vibrational spectroscopy, neutron scattering, free electron laser, light emitting diode, thermal quenching.*

List of publications

This thesis includes the following papers

I Inorganic Phosphor Materials for Lighting

Yuan-Chih Lin, Maths Karlsson, and Marco Bettinelli

Topics in Current Chemistry, **374**, 1–47, (2016)

doi: 10.1007/s41061-016-0023-5

II Local structure and vibrational properties of the yellow-emitting phosphor $\text{Y}_{3-x}\text{Ce}_x\text{Al}_5\text{O}_{12}$ ($x = 0 - 0.09$)

Yuan-Chih Lin, Paul Erhart, Marco Bettinelli, Stewart F. Parker, and Maths Karlsson

In manuscript

III Mode-selective vibrational excitation and relationship to thermal quenching in the yellow-emitting phosphor Ce^{3+} -doped $\text{Y}_3\text{Al}_5\text{O}_{12}$

Yuan-Chih Lin, Marco Bettinelli, Suchinder Sharma, A. F. G. van der Meer, Britta Redlich, Adolfo Speghini, and Maths Karlsson

In manuscript

Other papers to which I have contributed but that are not part of this thesis

i Structural and Vibrational Properties of Silyl (SiH_3^-) Anions in KSiH_3 and RbSiH_3 : New Insight into Si–H Interactions

Verina F. Kranak, Yuan-Chih Lin, Maths Karlsson, Janos Mink, Stefan T. Norberg, and Ulrich Häussermann

Inorganic Chemistry, **54**, 2300–2309, (2015)

doi: 10.1021/ic502931e

ii Vibrational properties of β - KSiH_3 and β - RbSiH_3 : a combined Raman and inelastic neutron scattering study

Janos Mink, Yuan-Chih Lin, Maths Karlsson, Carin Österberg, Terrence J. Udovic, Henrik Fahlquist, and Ulrich Häussermann

Journal of Raman Spectroscopy, (2016)

doi: 10.1002/jrs.5013

In Press

Contents

1	Introduction	1
2	Inorganic phosphors	5
2.1	General characteristics	5
2.2	Garnet type phosphors and YAG:Ce ³⁺	6
2.2.1	Crystal structure	6
2.2.2	Optical properties	8
2.2.3	Vibrational properties	11
2.3	Thermal quenching	12
2.3.1	Electron-phonon coupling	12
2.3.2	Thermal ionization	15
3	Experimental	17
3.1	Vibrational spectroscopy	17
3.1.1	Infrared spectroscopy	17
3.1.2	Raman spectroscopy	18
3.1.3	Inelastic neutron scattering	19
3.1.4	Phonon assignment by symmetry coordinates	20
3.2	Luminescence	22
3.2.1	Photoluminescence	22
3.2.2	Thermoluminescence	23
3.3	Free electron lasers	24
4	Instruments	27
4.1	The Bruker IFS 66v/s spectrometer	27
4.2	The Dilor XY 800 spectrometer	28
4.3	The TOSCA INS spectrometer	29
4.4	Photoluminescence and thermoluminescence experiments	30
4.5	The FELIX infrared free electron laser	31
5	Summary of results	33

6 Conclusions and outlook	35
Acknowledgments	37
Bibliography	39
Papers I–III	47

Glossary

LEDs	Light emitting diodes
RGB	Red, green, and blue
CCT	Correlated color temperature
CRI	Color rendering index
pcWLEDs	Phosphor converted white light emitting diodes
QE	Quantum efficiency
DFT	Density functional theory
EXAFS	Extended X-ray absorption fine structure
DOS	Density of states
CB	Conduction band
VRBE	Vacuum referred binding energy
IR	Infrared
INS	Inelastic neutron scattering
EM	Electromagnetic
PL	Photoluminescence
TL	Thermoluminescence
FEL	Free electron laser
RF	Radio frequency
FTIR	Fourier transform infrared
CCD	Charge coupled device
CW	Continuous wave
FELIX	Free Electron Laser for Infrared eXperiments
Linac	Linear accelerator

Chapter 1

Introduction

Lighting consumes as much as approximately one fifth of worldwide electricity [1, 2]. The enormous demand for lighting drives the rapid growth of the new and environment-friendly solid-state white lighting technologies that aim to replace the old and inefficient technologies that have been phased out (incandescent lamps) or are problematic from an environmental point of view (compact fluorescent lamps) [2]. The invention of bright-blue light emitting diodes (LEDs) [3, 4] in the mid-90s has led to the development of devices capable of producing white light in a reliable and efficient way, based on inorganic phosphors. These consist of a crystalline host lattice [*e.g.* $\text{Y}_3\text{Al}_5\text{O}_{12}$ (YAG)] and a small concentration of activator ions (*e.g.* the lanthanide Ce^{3+} , Pr^{3+} , and so forth), which convert light from the LED into longer wavelengths. The admixture of different wavelengths results in white light emission. Most commonly, blue LEDs ($\sim 450\text{--}480\text{ nm}$) can be used to excite either a yellow phosphor or a green and a red phosphor, whilst UV LEDs ($\sim 380\text{--}410\text{ nm}$) are used to excite red (R), green (G) and blue (B) phosphors, to produce white light, see Figure 1.1.

The lighting characteristics are typically defined by the correlated color temperature (CCT) and the color rendering index (CRI). The CCT is a measure of the perceived color temperature of the emitted light compared to that of black-body radiation such as from the sun. The CRI is a parameter indicating the capability to reproduce colors of an object with respect to that as illuminated by a black-body radiation source. A low CCT ($< 4000\text{--}5000\text{ K}$) and a high CRI (close to 100) yield a warm, natural and comfortable white light emission spectrum, generally suited for, *e.g.*, indoor lighting.

Currently, one of the most widely used phosphor converted white LEDs (pcWLEDs) on the market is the blue LED coated with the yellow-emitting phosphor Ce^{3+} -doped $\text{Y}_3\text{Al}_5\text{O}_{12}$ (YAG: Ce^{3+}), which can emit bright white light with a relatively high efficiency (up to 85 %) [6]. However, a major

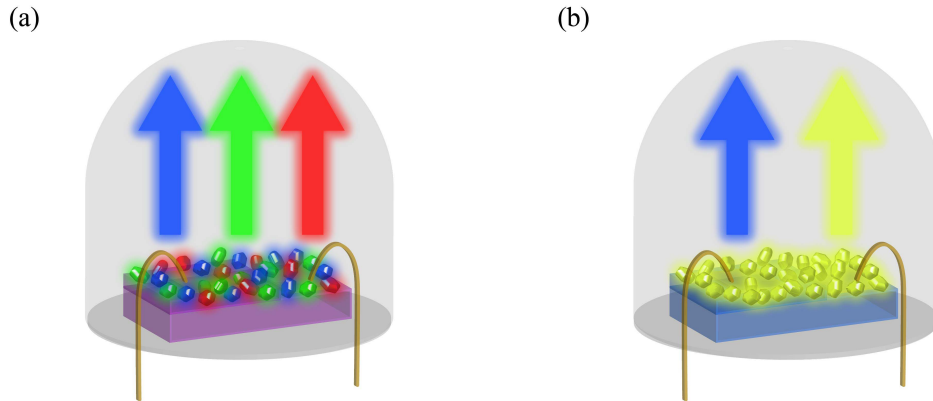


Figure 1.1: (a) An UV LED + RGB phosphors, and (b) a blue LED + a yellow phosphor, adapted from [5].

disadvantage of currently available devices is that the emitted white light has a strong blue component and hence is perceived as cold and unnatural. In comparison, UV LEDs coated with RGB phosphors produce a warmer white light, however these devices may suffer from technical complexity of mixing different phosphors onto LED chips, and low efficiency [7]. Furthermore, pcWLEDs generally suffer greatly from thermal quenching, *i.e.* a pronounced reduction in emission intensity or quantum efficiency (QE)¹ of the phosphors, observed at elevated temperature, typically a few hundred degree centigrade. To conclude, the trade-off between different measures, such as CCT, CRI, QE, cost, fabrication and so forth, always presents and it is hardly satisfactory in all aspects [5, 9].

In view of these materials challenges, which have hindered the development and widespread use of pcWLEDs, recent, promising research points toward that the lighting characteristics of inorganic phosphors can be modulated significantly by changing their short-range (local) crystal structure and vibrational characteristics [10]. In effect, this may provide a means to tune the light emission so that the emitted light is perceived as, *e.g.*, warmer and thus more suitable for indoor lighting, or so that the phosphor is more thermally stable. However, the correlation between optical properties, local structure, and vibrational dynamics of phosphors is not fully understood. For this reason, this thesis aims to clarify in detail how the local structure and dynamics of phosphors affect their optical properties, in particular in

¹QE is divided into internal and external. Internal QE = the number of emitted photons / the number of absorbed photons; External QE = the number of emitted photons / the number of incident photons. [8]

relation to emission wavelength and thermal quenching. The studies are focused on the technologically very important yellow phosphor YAG:Ce³⁺. The primary tools involve the use of infrared, Raman, luminescence, and neutron spectroscopies together with computer modeling based on density functional theory (DFT). Additionally, a new approach is used, that is the application of monochromatic infrared irradiation simultaneously with the electronic excitation of activator ions, for studying of how certain vibrational modes couple to luminescence.

Chapter 2

Inorganic phosphors

2.1 General characteristics

An inorganic phosphor consists of activator ions, which serve as luminescent centers, and a host lattice that accommodates the activator ions, see Figure 2.1(a). The activator ions convert light of a certain wavelength into light of a longer wavelength and heat. The energy conversion process involves transitions between electronic states as well as between vibrational states. This may be explained by a so called configurational coordinate diagram, as that shown in Figure 2.1(b). The electronic transition redistributes electrons from the ground state to the excited state. The excited-state electrons are often relaxed to lower vibrational states before returning to the electronic ground state, due to the much shorter lifetime of vibrational transitions (on the order of fs–ps) compared to electronic transitions (on the order of ns). The shapes and intensities of the absorption/excitation and emission spectra are determined by the square of the (vertical) overlap integrals of the vibrational wavefunctions of the ground and excited states. The overlap integrals are affected by the difference in nuclear coordinates between the ground- and excited-state parabolae, which depends on the difference in bonding forces between the ground and excited states. It can be concluded that the luminescence properties of inorganic phosphors depend on the electronic configuration of the activator ions, both in the ground and excited states, as well as on the vibrational properties of the activator ions and the host lattice in which they are incorporated.

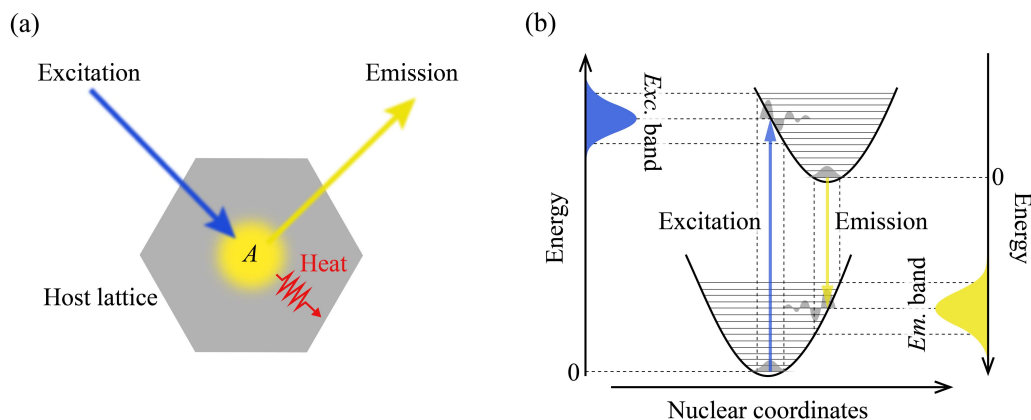


Figure 2.1: (a) A simple picture of a phosphor, which comprises one activator ion (A) embedded in a host lattice, adapted from [11]. (b) Schematic principle of luminescence plotted in a configurational coordinate diagram, adapted from [12]. *Exc.* and *Em.* stand for light excitation and emission, respectively.

2.2 Garnet type phosphors and YAG:Ce³⁺

2.2.1 Crystal structure

Although the nature of the luminescent ion contributes to the optical properties of phosphors, the structure and dynamics of the host lattice is also critically important. Examples of host matrices for generating yellow light emission are oxynitrides, silicates, and aluminates [5]. The most important class of hosts of technological interest is, however, oxide garnets, particularly Ce³⁺-doped ones [5]. For instance, the garnet families of aluminates (Y, Tb, Gd, Lu)₃Al₅O₁₂ [6, 13–15], silicates Ca₃Sc₂Si₃O₁₂ [16], and the more complex compositions, such as Y₃Mg₂Si₂AlO₁₂ [17], Y₃Sc₂Ga_{3-x}Al_xO₁₂ [18], Ca₂GdZr₂Al₃O₁₂ [19], and Lu₂CaMg₂(Si,Ge)₃O₁₂ [20] have been reported and their chemical formula can be generally expressed as $A_3B_2(XO_4)_3$, where A , B and X are cations located at distinct Wyckoff positions, and O is oxygen. Of specific concern for this thesis is the yttrium aluminium garnet, Y₃Al₅O₁₂ (YAG). The YAG crystal structure is built up of tetrahedra (AlO₄), octahedra (AlO₆), and 8-fold coordinated Y cations, as illustrated in Figure 2.2. It crystallizes into the space group $Ia\bar{3}d$ (O_h^{10}) [21], which is a body-centered cubic Bravais lattice, and its unit cell consists of 160 atoms. For the Ce³⁺-doped equivalent, YAG:Ce³⁺, the Ce³⁺ ions substitute for the Y³⁺ ions.

The local environment of the Y³⁺ ions in YAG, or equivalently Ce³⁺ in YAG:Ce³⁺, is shown in Figure 2.3(a). Since Ce³⁺ is larger than Y³⁺ the substitution for Ce³⁺ results in a local lattice expansion. Results obtained

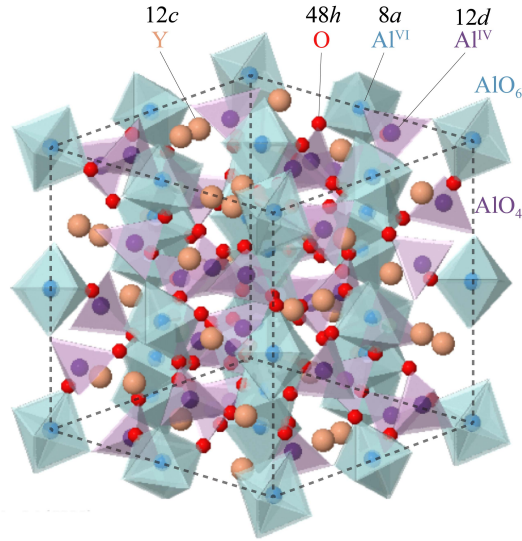


Figure 2.2: The unit cell of the YAG crystal, where the Y, Al^{VI} and Al^{IV} cations are situated at the Wyckoff positions 12*c*, 8*a* and 12*d*, respectively, and are coordinated dodecahedrally, octahedrally and tetrahedrally to the neighboring O anions which occupy the Wyckoff position 48*h*.

from extended X-ray absorption fine structure (EXAFS) experiments have shown that the lattice environment around the Ce³⁺ ions is expanded upon increasing Ce³⁺ doping and that the expansion ratio becomes smaller at outer shells [22, 23], implying that the distortion is local. However, even the first-shell expansion, *i.e.* the Ce–O bonds, is smaller than one would expect from the difference in ionic radii between Ce³⁺ and Y³⁺. It implies that the YAG lattice appears to be a rigid structure against Ce³⁺ doping [22]. In effect, the local structure around the Ce³⁺ ions in YAG:Ce³⁺ is somewhat compressed. In view of the averaged structure, the lattice expansion in YAG:Ce³⁺ follows a linear relationship with increasing Ce³⁺ concentration [22, 24, 25], see Figure 2.3(b).

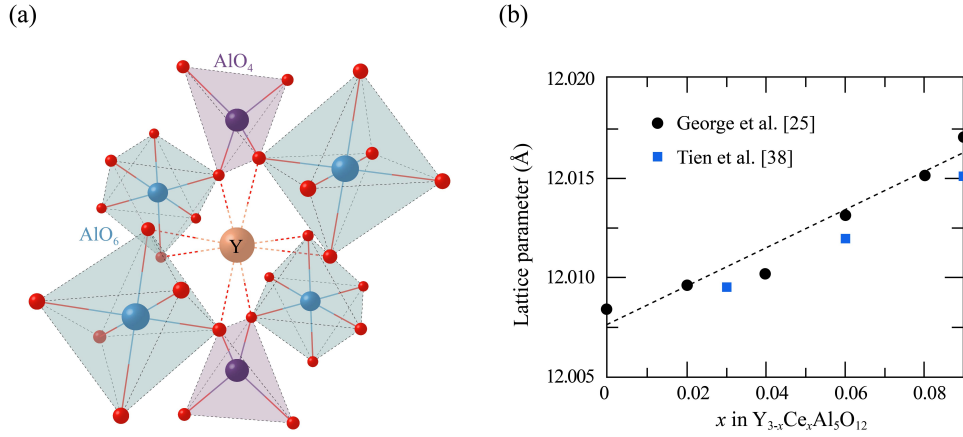


Figure 2.3: (a) The local structure around the Ce^{3+} ions in $YAG:Ce^{3+}$ illustrates that a CeO_8 moiety co-shares the O^{2-} ions with the adjacent four AlO_6 and two AlO_4 moieties. (b) Lattice expansion of $YAG:Ce^{3+}$ upon increasing Ce^{3+} concentration, adapted from [22].

2.2.2 Optical properties

The ground state electronic configuration of Ce^{3+} is $[Xe]4f^15d^0$. Typically, the Ce^{3+} luminescence originates from electronic transitions between the $4f^15d^0$ and $4f^05d^1$ states, namely $4f-5d$ transitions. The $4f-5d$ transition energy of the free Ce^{3+} ions is in the range of UV light (~ 6.12 eV), but is shifted by 3.41 eV [$D(A)$ in Figure 2.4(a)] to lower energies (in the range of visible light) when incorporated in the YAG crystal [26]. The local lattice environment mainly affects the outer shell of the Ce^{3+} ions, *i.e.* the $5d$ states, in terms of the covalency of the Ce–O bonds, and the ligand field [27]. The ligand field [28, 29] describes how the energies of the $5d$ orbitals of the Ce^{3+} ions are split due to the combined effects of the electrostatic (crystal) field created by the surrounding oxygens, and the interactions of the bonding orbitals. The Ce–O covalency effect, or equivalently the nephelauxetic effect results from the extensive overlap of the molecular orbitals of the Ce^{3+} ions and the coordinated O^{2-} ions, which increases the covalency of the Ce–O bonds and thereby gives rise to a large centroid shift ε_{cs} , *cf.* Figure 2.4(a). Since the Ce^{3+} ions coordinate to eight O^{2-} ions in a cubic-like geometry, the centroid shifted $5d$ states are firstly split into the triplet states ${}^2T_{2g}$ with higher energy and the doublet states 2E_g with lower energy. The energy difference between the ${}^2T_{2g}$ and 2E_g states is $(8/9) \cdot 10Dq$, where the coefficient $(8/9)$ is a coordination factor related to the cubal ligand field. The quantity of Dq can be approximated by the point charge model as,

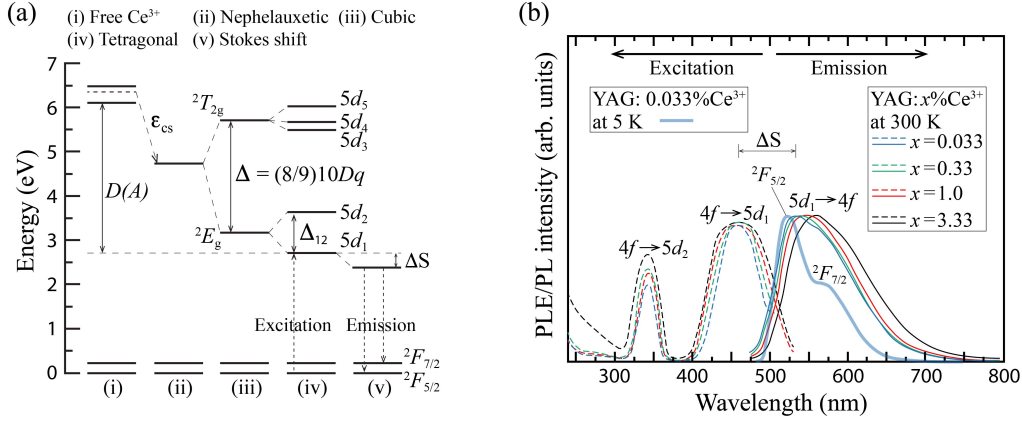


Figure 2.4: (a) The 4*f* and 5*d* electronic states of the Ce³⁺ ions in the free state as well as embedded in an oxide garnet, *e.g.* YAG, adapted from [26]. (b) Luminescence spectra of YAG:Ce³⁺, adapted from [33].

$$Dq = \frac{Ze^2r^4}{6R^5}, \quad (2.1)$$

where Z is the charge or valence of the anion, e is one electron charge, r is the radius of the 5*d*-orbital wavefunction, and R is the Ce–O bond length in YAG:Ce³⁺ [30–32]. Subsequently, the ²T_{2*g* and ²E_g states are further split into non-degenerate states because of the lowered symmetry (from the cubal to dodecahedral coordination) of CeO₈ in the garnet structure. The dodecahedral coordination results in a tetragonal ligand field. Since the Ce³⁺ 4*f*–5*d* transition in YAG:Ce³⁺ involves not only the Ce³⁺ electronic states but also the vibrational states, the Ce³⁺ 5*d* electrons relax to lower vibrational states by the Stokes shift Δ*S* of ~ 2000–4000 cm⁻¹ before they radiatively return to the 4*f* ground state. Δ*S* may be evaluated by the difference between the peak positions of the excitation and emission spectra [33, 34], see Figure 2.4(b). The Ce³⁺ 4*f* states are primarily affected by the spin-orbit coupling, which leads to a splitting of the 4*f* states into the ²F_{5/2} and ²F_{7/2} states which are separated by ~ 2000 cm⁻¹ in YAG:Ce³⁺ [29, 35]. The two emission bands corresponding to the ²F_{5/2} and ²F_{7/2} states have been observed in the low-temperature photoluminescence spectrum [Figure 2.4(b)].}

2.2.2.1 Relationship between optical properties and tetragonal lattice distortions of the CeO₈ moieties

An important result from luminescence data of the garnet phosphors Ce³⁺-doped (Gd, Y, Lu)₃(Al, Ga)₅O₁₂ is that the frequency of the emitted light

depends strongly on the strength of the tetragonal ligand field, that is the degree of tetragonal distortion of the nearly cubic CeO_8 moieties. In effect, the splitting energy Δ_{12} is changed [26], *cf.* Figure 2.4(a). In order to quantify/estimate the degree of tetragonal distortion, a distortion parameter has been defined by the ratio of the O–O distances between different edges of a YO_8/CeO_8 moiety, d_{88}/d_{81} , as shown in Figure 2.5(a). For instance, the substitution of the larger Ga for Al in the related garnet phosphors $(\text{Y}, \text{Gd})_3(\text{Ga}, \text{Al})_5\text{O}_{12}:\text{Ce}^{3+}$ enlarges the lattice dimension and the local CeO_8 turns into more cubic-like symmetry which reduces d_{88}/d_{81} as well as Δ_{12} and gives a blue shifting effect of the emitted light [36–38]. A similar blue shifting effect has been observed in another garnet phosphor, $\text{Y}_3\text{Sc}_2\text{Ga}_{3-x}\text{Al}_x\text{O}_{12}:\text{Ce}^{3+}$, as the Ga^{3+} content increases [18]. In contrast, a red shifting effect is enhanced when larger cations replace the cation situated at the D_2 site (equivalent to the Wyckoff position $12c$) in the series of $(\text{Y}, \text{Gd}, \text{Tb}, \text{Lu})_3\text{Al}_5\text{O}_{12}:\text{Ce}^{3+}$ [13, 14, 25] whose local bonding distances show the relation $\text{Gd-O} > \text{Tb-O} > \text{Y-O} > \text{Lu-O}$ [39]. The counteracting effect on Δ_{12} in terms of the lattice dimension is explained by that the CeO_8 moieties tend to be more tetragonally distorted when the D_2 site is occupied by larger cations. Similar results are also found in the Ce^{3+} and Li^+ co-doped $(\text{Ca}_{1-x}\text{Sr}_x)_3\text{RE}_2\text{Ge}_3\text{O}_{12}$ phosphors [10].

Intuitively, the elongation of the Ce–O bonds is expected to lead to a decreased tetragonal ligand field and hence a blue-shifted emission spectrum. The red-shift effect upon increasing Ce^{3+} concentration in $\text{YAG}:\text{Ce}^{3+}$ [Figure 2.4(b)], is thought to relate to energy transfer from the Ce^{3+} ions at higher $5d$ vibronic states to the nearby ones at lower energy states, as well as to enhanced ligand-field splitting of the Ce^{3+} $5d$ states due to the compressed local environment around the Ce^{3+} ions [22]. However, the observed red-shift could also relate to the dynamical properties of the system, as certain vibrational modes, such as symmetric compression and bending motions of the CeO_8 moiety [40, 41] [*cf.* Figure 2.5(b–c)], induce dynamical tetragonal distortions of the nearly cubic CeO_8 . Whatever the case, the effects of the local structural dynamics on the optical properties of $\text{YAG}:\text{Ce}^{3+}$ as well as on other phosphors, are not fully understood. Their investigation lays at the heart of this thesis.

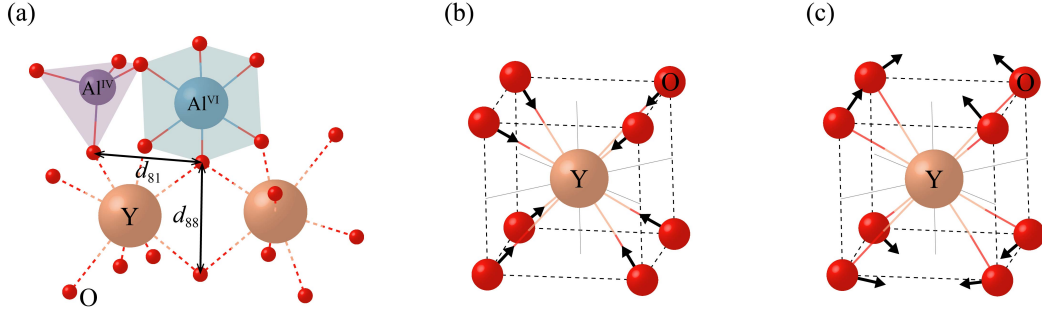


Figure 2.5: (a) Schematic illustration of the distortion parameter d_{88}/d_{81} at the D_2 site in YAG, adapted from [10]. (b–c) Schematic illustration of the local lattice distortions as induced by (b) symmetric stretching and (c) symmetric bending motions, respectively, adapted from [41].

2.2.3 Vibrational properties

Since the YAG primitive cell is half of the unit cell and thereby comprises 80 atoms, the three dimensional freedoms contributed from each atom lead to a total of 240 vibrational modes of the YAG structure. At the Γ -point in the Brillouin zone these modes can be denoted by their irreducible representation according to factor group analysis [42],

$$\Gamma = 5A_{1u} + 3A_{1g} + 5A_{2u} + 5A_{2g} + 10E_u + 8E_g + 14T_{1g} + 18T_{1u} + 14T_{2g} + 16T_{2u}, \quad (2.2)$$

where $3A_{1g} + 8E_g + 14T_{2g}$ and $17T_{1u}$ are the Raman- and IR-active vibrational species, respectively, $1T_{1u}$ is the acoustic motion, whereas the remaining species are optically silent modes. To correlate the vibrational species in Equation 2.2 with the site symmetries in the oxide garnets $A_3B_2(XO_4)_3$, the correlation method [43, 44] has been performed on the silicate garnets [45] and the result has assigned the vibrational species to the translatory motion of the cations A and B , and all types of the vibrations (translatory, rotatory and intra-molecular motions) of the tetrahedral XO_4 moiety. More specifically, the studies [42, 46–48] on the vibrational properties of the rare-earth aluminate garnets $RE_3Al_5O_{12}$ have revealed that the lattice vibrations are predominantly related to RE motions and motions of octahedral AlO_6 and tetrahedral AlO_4 moieties in the spectral range of low frequency ($\lesssim 300 \text{ cm}^{-1}$) and medium-to-high frequency ($\sim 300\text{--}1000 \text{ cm}^{-1}$), respectively, as seen in the one phonon density of states (DOS) [Figure 2.6].

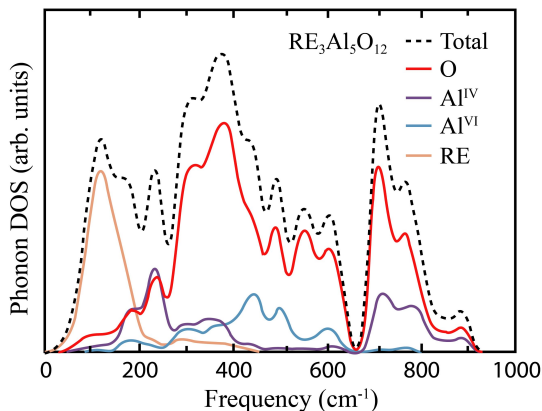


Figure 2.6: The one phonon DOS of $\text{RE}_3\text{Al}_5\text{O}_{12}$, adapted from [48].

2.3 Thermal quenching

Thermal quenching, *i.e.* the pronounced reduction in QE of phosphors at elevated temperature (see Figure 2.7), is primarily thought to be the result of two different processes, electron-phonon coupling and/or thermal ionization. These processes are briefly described in the following.

2.3.1 Electron-phonon coupling

Thermal quenching *via* electron-phonon coupling refers to the phenomenon that may occur when the excited-state electrons interact with phonons in such a way that the excited-state electrons may return to the ground state without sending out light, *i.e.* in a non-radiative manner. This process may be described by a configurational coordinate diagram [49], see Figure 2.8(a). The two parabola represent the $4f$ and $5d$ electronic levels of a Ce^{3+} ion, where the horizontal lines are the quantized vibrational states. Since when the electron in a Ce^{3+} ion is excited from the $4f$ to the $5d$ state and the electronic charge distribution of the Ce^{3+} ion becomes more attractive to the neighboring anions so that the luminescent center shrinks [50], the $5d$ parabola shifts in the nuclear coordinate by ΔR (< 0) with respect to the $4f$ parabola. ΔR is a critical measure of the strength of the electron-phonon coupling and can be estimated by the Huang-Rhys coupling constant S_{HR} [51] and further correlated to the Stokes shift [ΔS in Figure 2.4(a)], according

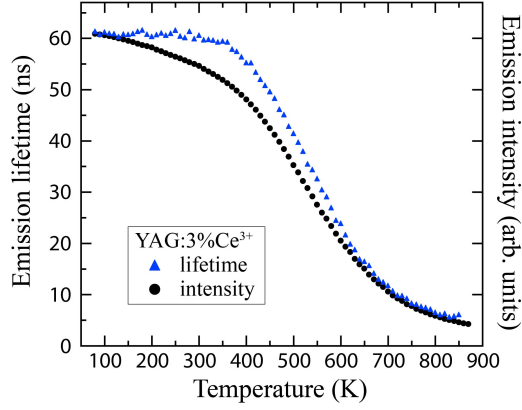


Figure 2.7: Temperature dependence of the emission intensity and lifetime of YAG:3%Ce³⁺, as measured in this thesis.

to [11, 32, 52]:

$$S_{\text{HR}} = \frac{1}{2} \frac{M\omega^2}{\hbar\omega} \Delta R^2 \simeq \frac{\Delta S}{2\hbar\omega}. \quad (2.3)$$

Here, M is the effective ionic mass and ω is the vibrational frequency of the phonon or local vibrational mode to which the excited-state electron couples with. To induce non-radiative relaxation, the excited $5d$ electrons have to couple with vibrational modes of energy $\geq \Delta E$, including higher-order transitions, *cf.* Figure 2.8(a). Besides, the symmetry and oscillating strength of the vibrations are decisive for the characteristics of non-radiative relaxation. As the requirements for $4f$ - $5d$ crossover are fulfilled, the Ce³⁺ $5d$ electrons return to the $4f$ ground state in a non-radiative way. The vibrational energy turns into heat dissipation in the lattice.

The rate of the non-radiative decay (R_{non} , s⁻¹) due to $4f$ - $5d$ crossover is given by,

$$R_{\text{non}} = A \cdot \exp^{-\Delta E/kT}, \quad (2.4)$$

where A is a rate constant of the order of 10¹³ s⁻¹, ΔE is the activation energy from the relaxed $5d$ state to the $4f$ - $5d$ crossing node, k is the Boltzmann constant and T is the temperature [53, 54]. Since the transition rate $R = R_{\text{rad}} + R_{\text{non}}$ (where R_{rad} is the radiative rate, which is usually independent of temperature) and the emission lifetime τ equals to $1/R$, the quantum efficiency (η) can be determined by the ratio τ/τ_0 [Equation 2.5]. τ can be expressed as Equation 2.6.

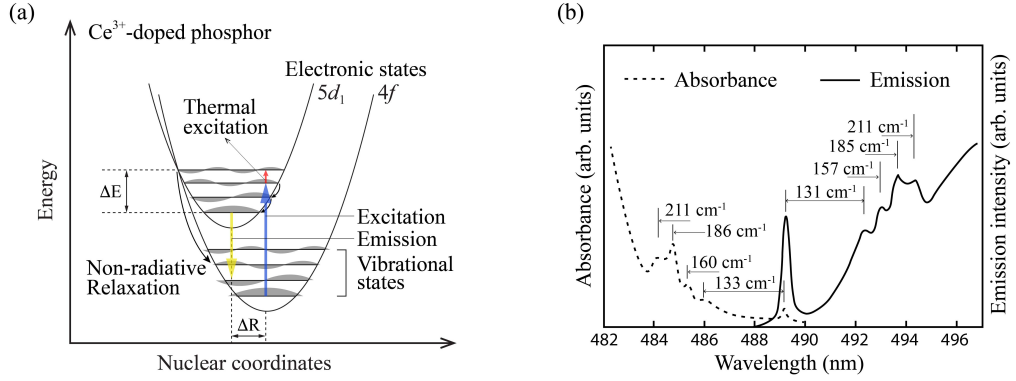


Figure 2.8: (a) Schematic illustration of the non-radiative relaxation process for Ce^{3+} -doped phosphors, *e.g.* $\text{YAG}:\text{Ce}^{3+}$. (b) The phonon side band structure of $\text{YAG}:\text{Ce}^{3+}$, adapted from [35].

$$\eta = \frac{\tau}{\tau_0} = \frac{1/(R_{rad} + R_{non})}{1/R_{rad}} = \frac{R_{rad}}{R_{rad} + A \cdot \exp^{-\Delta E/kT}} \quad (2.5)$$

$$\tau = \frac{1}{R_{rad} + A \cdot \exp^{-\Delta E/kT}} \quad (2.6)$$

τ_0 is the emission lifetime without any non-radiative relaxation involved. It follows that at a given ΔE , η and τ are enormously reduced when T is higher than T_Q .

From Figure 2.8(a), it can be seen that the larger ΔR is, the lower ΔE or T_Q one can expect and also the broader the luminescence bands are [53]. ΔR is comparatively large if the bonding force between the activator ion and the coordinated anions greatly changes when the activator ion is electronically excited. Therefore, $4f-5d$ transitions lead to a larger ΔR , as compared to that for the intra-configurational $4f-4f$ transition. Although the T_Q of $\text{YAG}:\text{Ce}^{3+}$ of the $4f-5d$ transition would have been low, the high rigidity of the YAG lattice reduces the population of the phonon modes at a given temperature and hence the $4f-5d$ crossover probability. Information about which particular phonon(s) that are actually at play may be indicated by the phonon side band structure in the luminescence spectra. The spectra in Figure 2.8(b) suggest that phonons of energies $\sim 200 \text{ cm}^{-1}$ may interact with the electrons of Ce^{3+} ions during the absorption/excitation and emission processes [33, 35].

2.3.2 Thermal ionization

Thermal ionization refers to the thermal promotion of electrons of the activator ions into the conduction band (CB) of the host crystal. This reduces the probability of radiative transitions, *e.g.* the $5d \rightarrow 4f$ transitions for Ce^{3+} ions, and hence luminescence lifetime (τ) and intensity. The occurrence of thermal ionization speeds up the transition rate R ($= \tau^{-1}$) of electrons by a non-radiative rate R_{ion} so that $R = R_{rad} + R_{ion}$, where $R_{ion} = A_{ion} \cdot \exp^{-\Delta E_{ion}/kT}$, and ΔE_{ion} and A_{ion} are the activation energy and rate coefficient of thermal ionization, respectively [12]. Figure 2.9(a) shows, as an example, the situation of thermal ionization when electrons at the excited state (e) are thermally promoted into the CB (by providing an energy of ΔE_{ion}), and then get trapped by a defect state. Defects in this sense can be, *e.g.*, impurities, oxygen vacancies, bound excitons and antisite defects [11, 55, 56]. The trapped electrons might be thermally released and promoted back to the CB, while still having a low probability of emitting radiatively [Figure 2.9(a)]. Figure 2.9(b) shows, for comparison, the case when the electrons are excited from the ground state (g) to the excited state (e) situated in the CB, and the delocalized electrons recombine with holes at a recombination center. This process is known as photoionization, which leads to strong or even complete luminescence quench [11].

Information about thermal ionization in phosphors can be obtained from measurements of the temperature dependent photocurrent [57, 58] and thermoluminescence (TL) [59]. An increased photocurrent and TL as a function of increasing glow intensity are a sign of thermal ionization in the material, which has been seen for, *e.g.*, Ce^{3+} -doped $\text{Y}_3\text{Al}_{5-x}\text{Ga}_x\text{O}_{12}$ (YAGG: Ce^{3+}). In particular, luminescence lifetime data [60, 61] and the so called vacuum referred binding energy (VRBE) scheme (*i.e.* binding energies relative to the vacuum energy) [26] of YAGG: Ce^{3+} , show that the higher the Ga substitution is, the probability for thermal ionization increases. However, thermal ionization has not yet been correlated to the reduction of luminescence lifetime on a quantitative scale or compared to other quenching mechanisms. Hence, the phenomenological existence of thermal ionization in inorganic phosphors needs to be further investigated to reflect on its importance in thermal quenching phenomena.

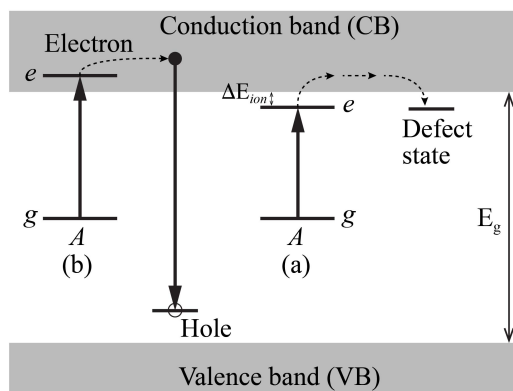


Figure 2.9: Schematic depiction of thermal ionization at the luminescent center A , for the cases when the electronic excited-state (e) is situated (a) below the CB (adapted from [57]), and (b) within the CB (adapted from [11]). E_g is the energy of the bandgap, and (g) is the ground state of A .

Chapter 3

Experimental

3.1 Vibrational spectroscopy

The vibrational spectra of materials can be investigated by infrared (IR) and Raman spectroscopies or by inelastic neutron scattering (INS), which each of them reveals the energy transitions between vibrational states. In the oversimplified case of a harmonic oscillator, the energy of the vibrational states of a specific mode may be expressed as $E_n \equiv (n + 1/2)h\nu$, where n is the quantum number (0, 1, 2, ...), ν is the vibrational frequency of the mode, and h is the Planck constant. The three techniques rely on different selection rules and, therefore, they are complementary to each other. For instance, vibrational modes that are inactive (silent) by photon excitation (*i.e.* by IR and Raman spectroscopies) may be observable in INS. Moreover, IR and Raman spectroscopies only measure zone-center (in the Brillouin zone) modes, whereas INS can probe vibrations at different wavevectors.

3.1.1 Infrared spectroscopy

IR spectroscopy measures the absorption of IR electromagnetic (EM) waves irradiated on a sample. The actual measurement may be performed in either of two different modes of operation, *i.e.* transmittance (absorbance) or reflectance. Figure 3.1(a) shows, as an example, the setup for a typical transmittance (absorbance) measurement, where I_r and I_s are the intensities of the IR light transmitting through the reference and sample, respectively, with a given IR frequency, ν_{ir} . Absorption occurs when the permanent electric dipole moment μ of a molecule, or vibrating moiety, oscillates at the identical frequency as that of the oscillating electric field of the incident IR light (*i.e.* at the resonance frequency, $\nu = \nu_{ir}$), which leads to the vibrational transition from, *e.g.*, $n = 0$ to $n = 1$, see Figure 3.1(b). An absorbance-like

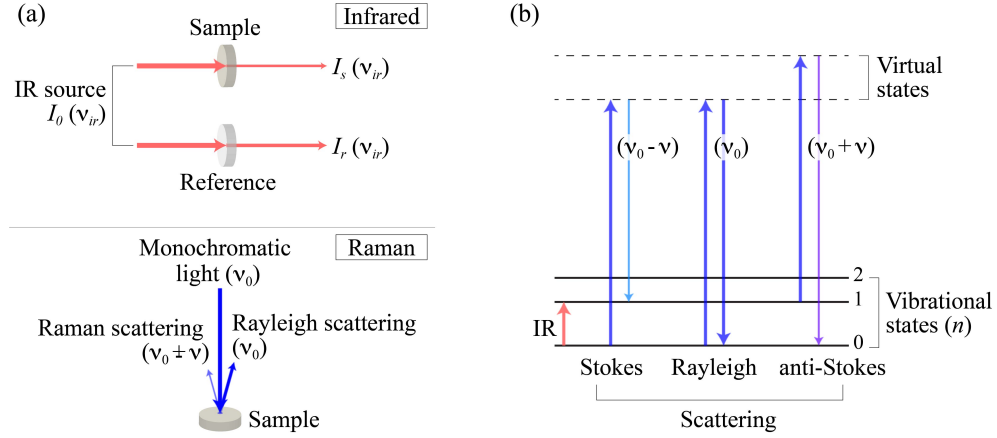


Figure 3.1: (a) Simple scheme for IR and Raman spectroscopies. (b) Energy transition processes for IR- and Raman-active vibrational modes.

spectrum can be obtained by taking the logarithm of the reference spectrum divided by the sample spectrum, *i.e.* $\log(I_r/I_s)$.

3.1.2 Raman spectroscopy

Raman spectroscopy measures the light scattered by the sample as illuminated by monochromatic light of frequency ν_0 , see Figure 3.1(a). The oscillating electric field $\varepsilon [= \varepsilon_0 \cdot \cos(2\pi\nu_0 t)$, where ε_0 is the maximum amplitude of the electric field] of the incident light induces a dipole moment μ_{ind} ($= \alpha\varepsilon$, where α is the polarizability) in the sample. If α oscillates around the equilibrium polarizability α_0 with the same frequency as that of a specific vibrational mode, *i.e.* $\alpha = \alpha_0 + \Delta\alpha \cdot \cos(2\pi\nu t)$ (where $\Delta\alpha$ is the maximum variation for α), μ_{ind} can be re-formulated as [62]

$$\mu_{ind} = \alpha_0\varepsilon_0\cos(2\pi\nu_0 t) + \frac{1}{2}\Delta\alpha\varepsilon_0\{\cos[2\pi(\nu_0 - \nu)t] + \cos[2\pi(\nu_0 + \nu)t]\}. \quad (3.1)$$

It can be seen that most light is scattered elastically with frequency ν_0 , *cf.* the first term in Equation 3.1. This is known as Rayleigh scattering. A small fraction of the light is scattered inelastically with frequency $\nu_0 - \nu$ (Stokes scattering) and $\nu_0 + \nu$ (anti-Stokes scattering), *cf.* the second and third terms in Equation 3.1, respectively. This is known as Raman scattering. The elastic and inelastic scattering occurs through the excitation to an intermediate virtual level, where the electronic wavefunctions are temporarily perturbed [44, 63], *cf.* Figure 3.1(b).

3.1.3 Inelastic neutron scattering

Inelastic neutron scattering (INS) uses neutrons rather than photons for obtaining a vibrational spectrum. In comparison to IR and Raman spectroscopies, both transferred energy ($\hbar\omega$, meV) and momentum (\mathbf{Q} , \AA^{-1}) are measured at the same time. The measured quantity is associated with the double differential scattering cross section, $d^2\sigma/(d\Omega dE_f)$, where $d\Omega$ is the solid angle ($= A_d/d_f^2$, as defined in Figure 3.2), and σ is the total scattering cross section (*i.e.* the number of neutrons scattered in all directions per second divided by the flux of the incident neutrons). $d^2\sigma/(d\Omega dE_f)$ can be written in terms of coherent and incoherent scattering functions, denoted by $S_{coh}(\mathbf{Q}, \omega)$ and $S_{inc}(\mathbf{Q}, \omega)$, according to

$$\frac{d^2\sigma}{d\Omega dE_f} = \frac{k_f}{k_i} \frac{\sigma_{coh}}{4\pi} S_{coh}(\mathbf{Q}, \omega) + \frac{k_f}{k_i} \frac{\sigma_{inc}}{4\pi} S_{inc}(\mathbf{Q}, \omega), \quad (3.2)$$

where $\omega = (E_i - E_f)/\hbar$ for an incident neutron energy of E_i and a final neutron energy of E_f , and σ_{coh} and σ_{inc} are the coherent and incoherent scattering cross sections, respectively [64,65]. In a crystal lattice, a local molecular motion (internal mode) is mostly probed by incoherent INS, whereas a collective lattice mode (external mode) is mostly measured by coherent INS [66,67]. For one specific atom (l), Equation 3.2 can be rewritten as

$$\left(\frac{d^2\sigma}{d\Omega dE_f}\right)_l = \frac{\sigma_l}{4\pi} \frac{k_f}{k_i} \frac{1}{2\pi\hbar} \sum_l \int_{-\infty}^{\infty} dt \langle e^{-i\mathbf{Q}\cdot\mathbf{r}_l(0)} e^{i\mathbf{Q}\cdot\mathbf{r}_l(t)} \rangle e^{-i\omega t}, \quad (3.3)$$

where $\mathbf{r}_l(t)$ is the time dependent position vector for the atom l [66]. Equation 3.3 can be further re-formulated in terms of the transition order n (0 for the elastic scattering; 1 for the fundamental transition; 2 for the first overtone, and so forth) and the atomic displacement \mathbf{u} of the ν -th vibrational mode, which is conventionally represented by $S^*(\mathbf{Q}, \omega_\nu)$ (related to the amplitude and cross section weighted density of states) in the spectrum as shown in Equation 3.4 [66].

$$S^*(\mathbf{Q}, \omega_\nu)_l^n \propto \sigma_l \frac{[(\mathbf{Q} \cdot \mathbf{u}_{\nu,l})^2]^n}{n!} \exp[-(\mathbf{Q} \cdot \sum_{\nu} \mathbf{u}_{\nu,l})^2] \quad (3.4)$$

The observed intensity in the INS spectrum is proportional to the summation of $S^*(\mathbf{Q}, \omega_\nu)_l^n$ over all the atoms in the material.

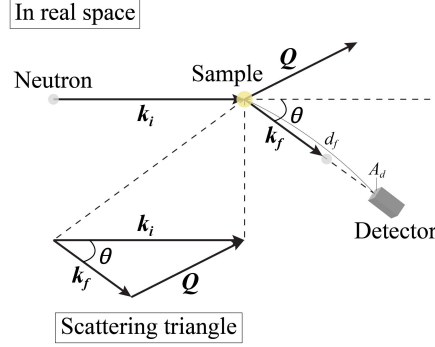


Figure 3.2: A scattering process between neutrons and a substance. θ is the scattering angle, k_i and k_f are the wavevectors of the incident and scattered neutrons, respectively, and Q is the transferred momentum (or the scattering vector), adapted from [66].

3.1.4 Phonon assignment by symmetry coordinates

For a crystal containing N atoms in the primitive cell, there are $(3N-3)$ optical-mode and 3 acoustic-mode lattice vibrations. Generally, the total $3N$ vibrations can be represented by the normal coordinates Q_i , which give the vibrational frequency ν_i and phase δ_i for the i th mode ($i = 1, 2, \dots, 3N$). The oscillation of all nuclei in a crystal can be expressed by $Q_i = Q_i^0 \sin(2\pi\nu_i t + \delta_i)$, where Q_i^0 is the maximum amplitude of the vibration. Since the 3 acoustic modes exhibit translational motions of the primitive cell as a whole (*i.e.* the center of gravity is stationary), these modes are usually not considered as using Q_i . Therefore, for a crystal of N atoms, $(3N-3)$ normal modes/vibrations may be represented by Q_i . The Q_i can be transformed into the mass-weighted Cartesian coordinates q_k as,

$$q_k = \sum_i B_{ki} Q_i^0 \sin(2\pi\nu_i t + \delta_i), \quad (3.5)$$

where B_{ki} is a coefficient for the coordination transformation. Physically $q_k = \sqrt{m_k} \Delta d_k$, where m_k is the mass of the nucleus and Δd_k is the displacement of the nucleus in one of the x -, y - and z -directions. The correlation between q_k and Q_i reveals that the motion of an nucleus is a superposition of all normal modes [44]. Equation 3.5 also indicates that if only a single normal mode ($i = j$) is considered, all nuclei vibrate in phase with the identical ν_j and δ_j , as generalized by $q_{kj} = B_{kj} Q_j^0 \sin(2\pi\nu_j t + \delta_j) = B_{kj} Q_j$. Furthermore, the collective motions of q_{kj} (the j th-mode phonon) can be correlated to the discrete vibrational levels [$E_{n_j} = (n_j + 1/2)h\nu_j$] in the quantum mechanics frame by plotting E_{n_j} in a potential parabola with respect to Q_j , namely

the configurational coordinate diagram [*e.g.* Figure 2.8(a)], and classically the quantum number n_j means the number of the j th-mode phonon. In this thesis, the eigenvalues (ν_j) and eigenvectors (q_{kj}) are obtained by using density functional theory (DFT) calculations.

To assign the phonon in terms of local motions which are determined by the symmetries of the local molecules in the crystal, the displacing vectors ($q_k/\sqrt{m_k}$) of the local molecule are decomposed into a linear combination of the translational, rotational and intra-molecular motions. Since the translational and rotational motions only change the spatial position of the molecule with respect to the reference frame, the structural symmetry of the molecule does not vary with such motions. However, for the intra-molecular motions, the molecular bonds vibrate in different symmetries which are based on the irreducible representations of the point group of the molecule, and these molecular vibrations can be expressed by the symmetry coordinates S_l in terms of the internal coordinates Δs as

$$S_a = \sum_R R \cdot \chi_a^R \cdot \Delta s, \quad (3.6)$$

where a and R stand for the irreducible representations and the symmetry operations of the point group of the molecule, respectively, χ_a^R is the character value for the irreducible representation a under the symmetry operation R , and Δs is the internal coordinates defined by the bonding length r and angle θ (corresponding to stretching and bending vibrations, respectively) [62]. To graphically illustrate this, Figure 3.3 shows the molecular vibrations of the A_{1g} stretching for the cubic YO_8 moiety [68], the doubly degenerate E_g stretching for the octahedral AlO_6 moiety [69], and the triply degenerate T_2 bending for the tetrahedral AlO_4 moiety [44]. Their symmetry coordinates are shown in Equation 3.7.

$$\begin{aligned} \text{Figure 3.3(a): } A_{1g}^r &= \Delta(r_1 + r_2 + r_3 + r_4 + r_5 + r_6 + r_7 + r_8) \\ \text{Figure 3.3(b): } E_g^r &= \Delta(r_1 + r_2 - 2r_3 + r_4 - 2r_5 + r_6) \\ \text{Figure 3.3(c): } T_2^\theta &= \Delta(\theta_{12} + \theta_{13} + \theta_{14} - \theta_{23} - \theta_{24} - \theta_{34}) \end{aligned} \quad (3.7)$$

It can be noted that the free-state molecules shown in Figure 3.3 are highly symmetric and their point groups are assigned by O_h for the cubic and octahedral molecules and by T_d for the tetrahedral molecule. However the structural symmetries of molecules generally become lowered when they are in the crystalline state and they are known as the site symmetries in crystals, *e.g.* in YAG, the site symmetries of YO_8 , AlO_6 and AlO_4 molecules are D_2 , S_6 and S_4 , respectively. Since lattice vibrations (phonons) are primarily

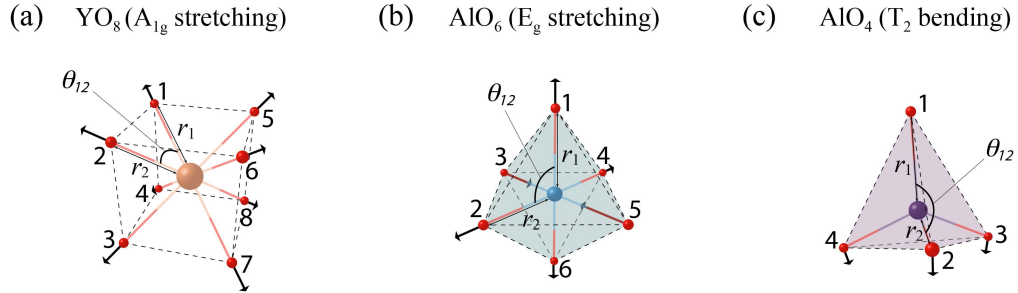


Figure 3.3: The symmetry coordinates of (a) A_{1g} stretching for a cubic YO_8 moiety, (b) E_g stretching for an octahedral AlO_6 moiety, and (c) T_2 bending for a tetrahedral AlO_4 moiety.

determined by the site symmetry and space group of a crystal, the phonon assignment with using the symmetry coordinates of free-state molecules is an approximate method for probing the local vibrational symmetries in a crystal lattice.

3.2 Luminescence

3.2.1 Photoluminescence

Photoluminescence (PL) of phosphor materials produces spontaneous emission of photons as light impinges on the phosphors. The excitation and emission processes may be described graphically by a configurational coordinate diagram, as depicted in Figure 2.1(b). The intensities of the two processes depend on the transition probability between vibronic levels, which leads to band-like distributions for the absorption and emission spectra, respectively. The frequencies of the absorbed and emitted light are mainly characterized by the electronic energy levels of the activator ions. In most cases, the emission spectrum is shifted to lower energies with respect to the excitation/absorption spectrum. The energy shift $\Delta (= h\nu_{\text{abs}} - h\nu_{\text{emi}}$, where ν_{abs} and ν_{emi} are the frequencies of the excited and emitted light, respectively) is a measure of the Stokes shift which in turn is correlated to the shift between the ground and excited electronic levels. An increased Stokes shift generally enhances electron-phonon coupling, which in turn broadens the spectral bands.

To investigate the time dependent photoluminescence of phosphors, a pulsed wave light is used as the excitation source. The light pulses promote

electrons of population density N_0 from the ground to excited states at the optical center. The population evolves with time, t , according to

$$N(t) = N_0 e^{-A_T t}, \quad (3.8)$$

where A_T is the total decay rate, *i.e.* the summation of the radiative and non-radiative rates [70]. The radiation intensity $I(t)$, observed by a photon detector, is proportional to $dN(t)/dt$, *i.e.* $I(t) = I(0)e^{-A_T t}$. Therefore, the luminescence lifetime τ ($= 1/A_T$) can be estimated from the time-dependent emission decay curve.

3.2.2 Thermoluminescence

Thermoluminescence (TL) occurs *via* a recombination process of electron-hole pairs when a substance, that previously absorbs energy from light excitation, is thermally stimulated. Energy may be charged into trapping (defect) states by optical excitation. More specifically, light may ionize the substance so that electrons and holes are created respectively in the conduction and valence bands. The carriers (the delocalized electrons and holes) might then get trapped at trapping states within the band gap, see Figure 3.4. The trapping states can result from intrinsic defects, such as lattice imperfections, or extrinsic defects, such as impurity contamination.

Since the carrier trapping at defects is at a non-equilibrium state, which is energetically metastable, the metastable state leads to an attempt to return to an equilibrium state by the annihilation of the electron-hole pairs, resulting in so-called TL glow. For a typical annihilation process, the trapped electrons are firstly promoted from the defect levels to the conduction band by coupling with thermally activated phonons. Subsequently, the promoted electrons recombine with the trapped holes at the recombination center. However, the annihilation might not occur if the promoted electrons in the delocalized conduction band are re-trapped by the defects. Consequently, TL glow intensity, which depends on the annihilation rate, is primarily determined by the dynamical process of electron de-trapping, electron re-trapping and electron-hole recombination. The first-order kinetics for TL intensity assumes that the effect of electron re-trapping is negligible. The TL intensity can then be written as

$$I(t) = -\frac{dn}{dt} = n \cdot s \cdot \exp^{-E/kT} = n \cdot R_{de}, \quad (3.9)$$

where n is the concentration of the trapped electrons, s is the frequency factor in the order of phonon frequency ($\sim 10^{12}$ – 10^{14} s⁻¹), E is the energy

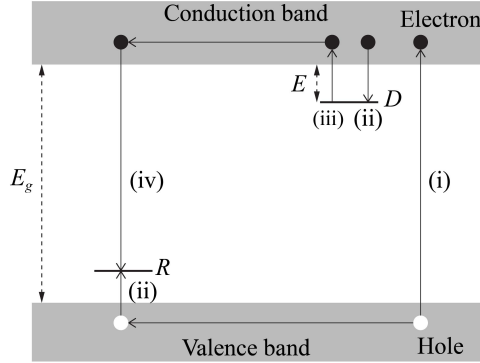


Figure 3.4: Energy band diagram for the one-trap TL model with the steps i) optical excitation, ii) carrier trapping, iii) electron de-trapping, and iv) electron-hole recombination, adapted from [71]. D is the defect, and R is the recombination center.

difference between the CB minimum and the electron trapping level, k is the Boltzmann constant, T is the temperature, and R_{de} is the de-trapping rate for one electron [71]. As T is varied linearly by a constant heating rate β , Equation 3.9 can be re-formulated as a function of temperature, see Equation 3.10 [71]. The maximum of TL intensity can be found at the temperature T_m with given s , β and E via Equation 3.11 which is derived from the relation $d \ln I(T)/dT = 0$ [71]. However, in practice, Equation 3.11 is frequently used for evaluating E instead of T_m .

$$I(T) = -\frac{1}{\beta} \frac{dn}{dt} = n_0 \cdot \frac{s}{\beta} \cdot \exp\left(-\frac{E}{kT} - \frac{s}{\beta} \cdot \int_{T_0}^T \exp^{-E/kT'} dT'\right), \quad (3.10)$$

$$\frac{\beta E}{kT_m^2} = s \cdot \exp^{-E/kT_m}, \quad (3.11)$$

where n_0 and T_0 are n and T at $t = 0$, respectively.

3.3 Free electron lasers

In a free electron laser (FEL), electrons are accelerated by a radio frequency (RF) linear accelerator (linac) to a relativistic speed, *i.e.* close to the speed of light. The electrons are grouped into sub-bunches of ps duration with a repetition rate of the order of GHz, which in turn are encapsulated into bunches of μ s duration separated by some hundreds of ms. The bunches are guided into a cavity comprising two high-reflectivity golden mirrors at the

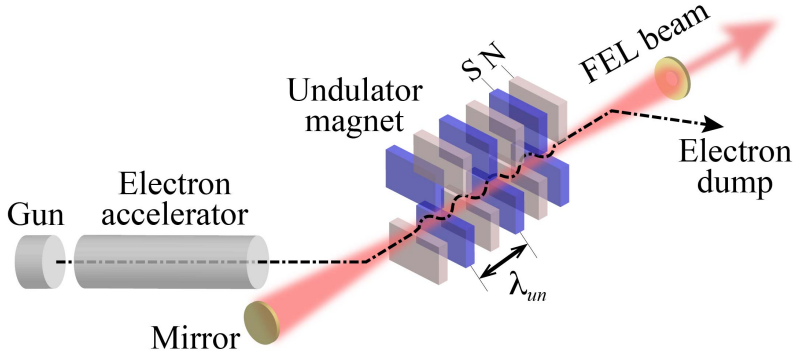


Figure 3.5: Schematic illustration of the working principle of a FEL, adapted from [72].

two ends which contain in between an undulator, *i.e.* a series of pairs of permanent magnets with periodically alternating magnetic poles, *cf.* Figure 3.5. The undulator transversely accelerate electrons so that electrons propagate along the undulator in zigzag, which results in synchrotron radiation due to the radial acceleration of electrons. While the radiation propagates more forwardly by an integer number (n , so called harmonic number [72]) of the radiation wavelength with respect to the electrons, the electrons are in resonance with the radiation. The resonance condition results in a spontaneous emission, which is, however, incoherent radiation. The wavelength (λ) of the spontaneous emission can be expressed as

$$n\lambda = \frac{\lambda_{un}}{\gamma} \frac{1}{2\gamma} (1 + K^2) = \frac{\lambda_{un}(1 + K^2)}{2\gamma^2}, \quad (3.12)$$

where λ_{un} is the periodic distance of the magnetic structure of the undulator, γ is the Lorentz factor ($=1/\sqrt{1-\beta^2}$, $\beta \equiv v/c$, v is the electron velocity and c is the speed of light), and K is a dimensionless parameter which is proportional to the magnetic field B [73, 74].

Since the electric field of the radiation interacts with the oscillating electrons, energy is exchanged between the radiation field and the electrons. The electrons propagate with a faster speed if energy is transferred from the radiation field to the electrons and vice versa. As a result, the forward-drifting electrons from the lagged electron group catch up with the backward-drifting electrons from the advancing electron group. The electrons bunch together periodically on the order of the wavelength of the radiation so that the radi-

ation can be amplified by the coherent spontaneous emission radiated from the bunched electrons. To acquire an amplification gain, the initial electron velocity is for instance biased by a small forward velocity, which leads to an off-resonance condition, and in this condition the radiation averagely extracts a net energy from the bunched electrons. The off-resonance gain is called the small-signal gain, which enhances the radiation power gradually as the radiation wave cycles in the cavity until the power reaches saturation. To conclude, a FEL provides a powerful and fast-pulsed monochromatic source, which for example is useful for performing time-resolved experiments on vibrational dynamics in relation to luminescence properties of inorganic phosphors.

Chapter 4

Instruments

4.1 The Bruker IFS 66v/s spectrometer

For the IR spectroscopy measurements reported in this thesis, I used a Fourier transform infrared (FTIR) spectrometer of the model Bruker IFS 66v/s. A key component of a FTIR spectrometer is the interferometer, which contains four major optical elements, a collimating mirror, a beam splitter, a fixed mirror and a moving mirror [Figure 4.1(a)]. The collimating mirror is used to collimate the incoming IR light, which is then partially reflected and transmitted by the beam splitter. The reflected and transmitted IR beams propagate respectively toward the fixed and moving mirrors, which reflect the IR beams back to the beam splitter where they are recombined into one beam. Since the traveling distance is fixed for the beam propagating between the beam splitter and the fixed mirror but not for the beam traveling to the moving mirror, the reflected and transmitted beams travel with an optical path difference, δ . This results in an interference pattern, also known as an interferogram. The interferogram is manifested by a combination of constructive and destructive interference. The interference depends on δ and the wavelength (λ) of the IR light, and it is recorded as a function of δ . Each λ is transformed into a cosine wave with a Fourier frequency in real space. The Fourier frequency is correlated with the velocity of the moving mirror, and the λ of the IR light [75]. The interferogram shows the summation of all such cosine waves. Therefore, any λ absorption by a sample reduces the amplitude of the interferogram, which is recorded by a detector situated behind the sample. Then, the recorded interferogram is Fourier transformed into a transmittance spectrum [I_r for the reference, or I_s for the sample, as shown in Figure 4.1(b)]. The vibrational spectrum is usually presented as absorbance, *i.e.* $A = \log(I_r/I_s)$, see Figure 4.1(b).

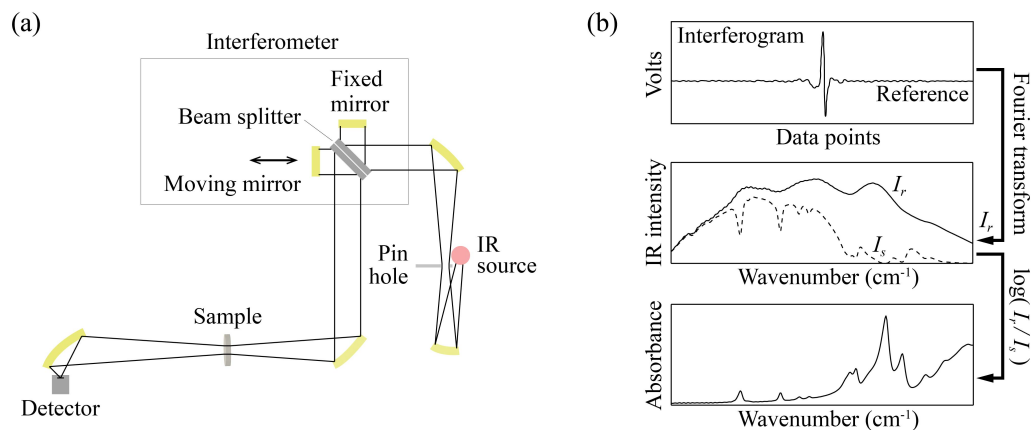


Figure 4.1: (a) Schematic layout of the Bruker IFS 66v/s spectrometer. (b) An interferogram, the transmittance spectra of the reference and sample, and the vibrational spectrum.

4.2 The Dilor XY 800 spectrometer

For the Raman spectroscopy measurements performed in this thesis, I used a triple-grating Dilor XY 800 spectrometer. The Dilor XY 800 spectrometer is equipped with a tunable Ar^+/Kr^+ laser, which produces an intense light that is linearly polarized. The linearly polarized light enters a microscope, which focuses the incident beam onto a sample. The backscattered light is guided through the entrance slit, S_1 , of the triple grating system, see Figure 4.2. From this point, the optical path depends on the setup of the spectrometer. In this thesis, the so called double subtractive mode was used. In this mode, the polychromatic light coming from the sample is dispersed by the first grating, G_1 , and then led to propagate through the second slit, S_2 . Here, S_2 acts as a bandpass filter, *i.e.* only light of specific wavelengths can enter the next stage, and thereby the width of S_2 determines the spectral range for detection. In the second stage, the light is merged by the second grating, G_2 , and then focused onto the slit S_3 , which rejects stray light. In the third stage, the polychromatic light is dispersed by the third grating G_3 and projected onto a charge-coupled device (CCD) detector cooled by liquid nitrogen. In short, the first and second stages work as a sharp bandpass filter, which significantly reduces stray radiation [76], and thus spectra can be measured close to the laser (Rayleigh) line. The third stage resolves the polychromatic light so that the dispersed light in a wide spectral range can be measured at once by an array detector, *i.e.* the scanning time for a desirable spectral window is shortened.

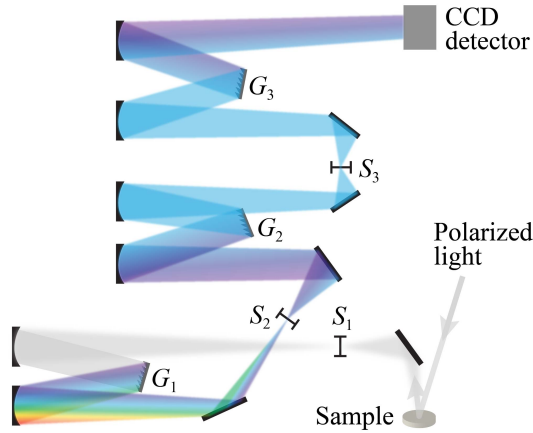


Figure 4.2: Schematic layout of the Dilor XY 800 Raman spectrometer.

4.3 The TOSCA INS spectrometer

For the INS spectroscopy measurements performed in this thesis, I used the TOSCA spectrometer as located at the ISIS Pulsed Spallation Neutron Source at the Rutherford Appleton Laboratory in the U.K. On TOSCA, the sample and analyzer module are placed in a configuration so that the neutrons are inelastically backscattered by the sample through a constant angle of 45° or 135° , see Figure 4.3. The backscattered neutrons then strike on a graphite crystal analyzer which only allows one wavelength of the neutrons to be Bragg scattered with a given interplanar distance in the crystal [77]. Subsequently, the neutrons pass through a longpass beryllium filter and arrive at the detector. Only neutrons within a narrow energy range can be detected, meaning that the final energy of the neutrons is essentially constant. The difference in energy and momentum, as determined by time-of-flight, between the incoming and detected neutrons determines the vibrational energy ω_ν and the scattering vector \mathbf{Q} (*cf.* Equation 3.4). Since the spectral intensity would be significantly reduced at high temperatures due to thermal motion, which is reflected by $\sum \mathbf{u}$ shown in the exponential term (Debye-Waller factor) in Equation 3.4, the measurement is usually performed at < 50 K.

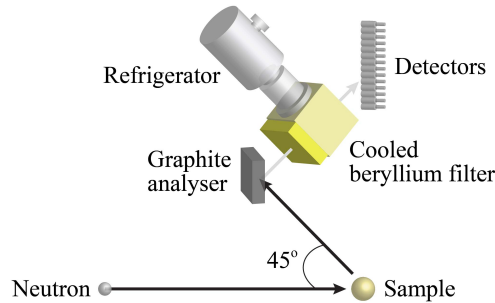


Figure 4.3: The analyzer module of TOSCA, adapted from [77].

4.4 Photoluminescence and thermoluminescence experiments

For the photoluminescence (PL) and thermoluminescence (TL) measurements, I used a home-built optical setup. This is depicted in Figure 4.4(a). PL spectroscopy measurements rely on a continuous-wave (CW) source for excitation, whereas the measurements of PL decay curves need a pulsed source. To collect the emission spectrum, a commercial spectrometer (Ocean optics USB2000+) working in the ultraviolet and visible (UV-VIS) regions was utilized (with an optical filter). The most critical component of the spectrometer is the grating, which diffracts the light toward a focusing mirror that projects it onto a CCD detector [Figure 4.4(b)]. In contrast, the luminescence decay curve was measured by a fast photon detector (Hamamatsu H10721-20).

For the TL measurements, the sample was firstly illuminated by an excitation source at a charging temperature for a certain time period. Thereafter, it was rapidly (*e.g.* 100 K/min) cooled down to a low temperature (*e.g.* 300 K, which was the initial temperature before it increased to the charging temperature) to trap the charges at defect states. Upon increasing the temperature with a constant heating rate, the TL glow curve was measured by a photosensor (Hamamatsu H10721-20). The temperature was manipulated by a heating/cooling stage (Linkam THMS600).

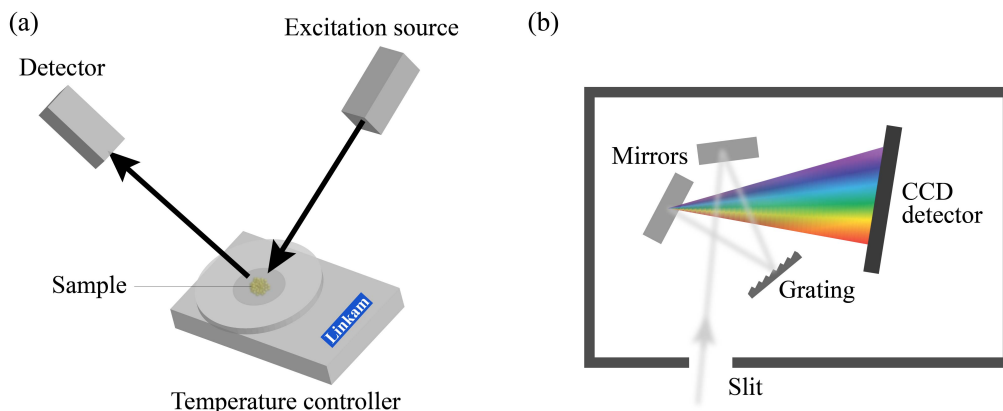


Figure 4.4: Schematic layouts of (a) the optical setup as used for the PL and TL experiments and (b) the Ocean optics USB2000+ spectrometer, adapted from [78].

4.5 The FELIX infrared free electron laser

For the experiments dealing with mode-selective vibrational excitation, I used the Free Electron Laser for Infrared eXperiment (FELIX) facility, as located in Nijmegen in the Netherlands. FELIX produces electron pulses of 1 GHz. The pulses are accelerated by linear accelerators (linac-1 and linac-2) to energies of 15–25 and 25–45/50 MeV [79, 80], as shown in Figure 4.5(a). The electrons accelerated by linac-1 and linac-2 are guided into two different cavities (FEL-1 and FEL-2), which comprise undulators and two golden mirrors placed at both ends of each cavity. The zig-zag propagation of electrons in the undulators results in spontaneous radiation, which becomes coherent due to energy exchange and stabilization between the radiation and electrons. The radiation is amplified by cycling it in undulators, which is then guided to the user stations.

The radiation wavelength can be modulated by varying the distance between the permanent magnets, *i.e.* adjusting the dimensionless K parameter (the magnetic field \mathbf{B}), *cf.* Equation 3.12. The IR pulses are tunable in the wavelength ranges of 30–150 μm (333–66 cm^{-1}) for FEL-1 and 3–45 μm (3333–222 cm^{-1}) for FEL-2 [80]. Figure 4.5(b) illustrates the FELIX pulse structure, which consists of macro pulses of 5–10 s length with a repetition rate of 10 Hz (*i.e.* a cycle period of 100 ms). Each macro pulse is built up of micropulses with a pulse length of *ca.* 1 ps and a repetition rate of 1 GHz, *i.e.* intervals of 1 ns. Each micropulse carries an energy of 1–20 μJ , thus *ca.*

100 mJ for each macropulse [80]. To investigate the mechanism of thermal quenching *via* electron-phonon coupling in the Ce^{3+} -doped phosphors, the sample is simultaneously excited by the FELIX beam (phonon excitation, in $250\text{--}1000\text{ cm}^{-1}$) and a blue pulsed laser (electronic excitation) [see Figure 4.5(a)].

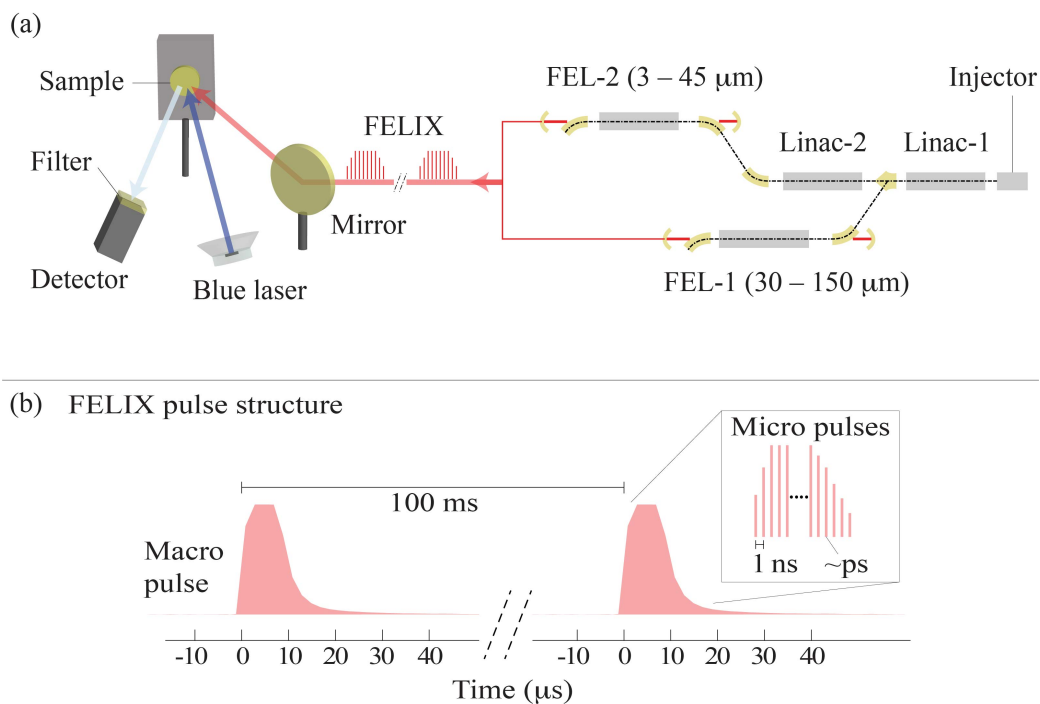


Figure 4.5: (a) Schematic layout of FELIX and the setup for the experiments of excitation by FELIX and a blue laser. (b) The pulse structure as generated by FELIX.

Chapter 5

Summary of results

The results in this thesis are reported in two papers, Paper II (Figure 5.1) and Paper III (Figure 5.2). Paper II reports on a comprehensive analysis of the vibrational properties of YAG and its relationship to luminescence of YAG:Ce³⁺. A key result is the assignment of all vibrational modes, on the basis of symmetry coordinates, *i.e.* the symmetries and amplitudes of all (YO₈, AlO₆, and AlO₄) moieties in terms of stretching and bending vibrations, respectively. The dependence of vibrational properties on Ce³⁺ concentration and temperature has also been elucidated. For example, we have shown that the vibrational motions of the CeO₈ moieties lead to pronounced tetragonal distortions that in turn induce a red-shifting effect on the Ce³⁺ emission. However, at temperatures higher than the Debye temperature, a counteracting effect on the light emission is observed, which is attributed to the thermal lattice expansion that makes the distorted CeO₈ moieties more cubic-like. Building on these new results, we have, in Paper III, investigated how the activation of specific vibrational modes affect the lifetime and intensity of the luminescence. This has been done by employing, for the first time, mode-selective vibrational excitation combined with optical excitation. The results show that the activation of the high-frequency IR-active phonons indeed gives rise to an additional decrease in the emission lifetime and intensity. This suggests that the high-frequency phonons are coupled with the Ce³⁺ excited electrons, which induce non-radiative relaxation *via* the 4*f*-5*d* crossover. But in addition, the TL glow curves of YAG:Ce³⁺ reveal that the Ce³⁺ excited electrons are thermally ionized and trapped by defect states. A lower activation energy obtained from the TL experiments, as compared to that shown in the VRBE scheme, suggests that the thermally-activated charge migration may be also involved in charge trapping. The contributions of electron-phonon coupling and thermal ionization to the reduction in the emission efficiency of YAG:Ce³⁺ are dependent on temperature in an Arrhe-

nius manner. Based on their activation energies, electron-phonon coupling ($\Delta E_{4d-5d} \sim 0.24$ eV) has shown to be more dominant than thermal ionization together with thermally-activated charge migration ($\Delta E_{ion} \sim 0.38$ eV), at lower temperatures, and *vice versa*.

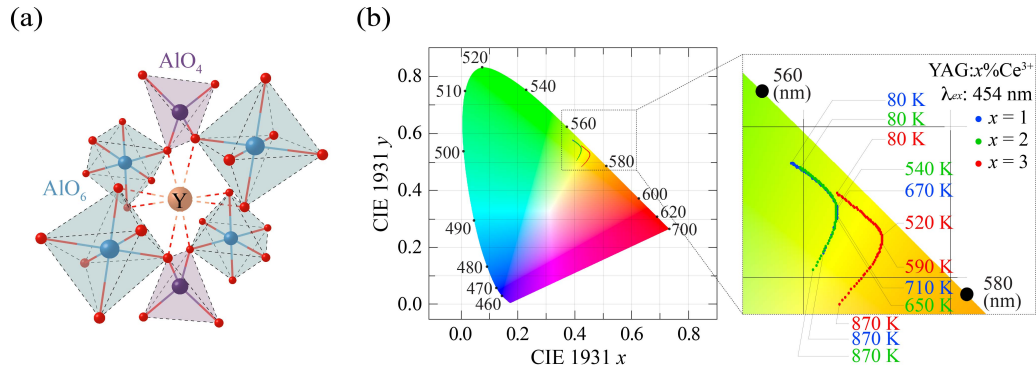


Figure 5.1: (a) Local structural environment of Y^{3+} in YAG, and (b) the temperature dependent chromaticity coordinates of $YAG:Ce^{3+}$, adapted from Paper II.

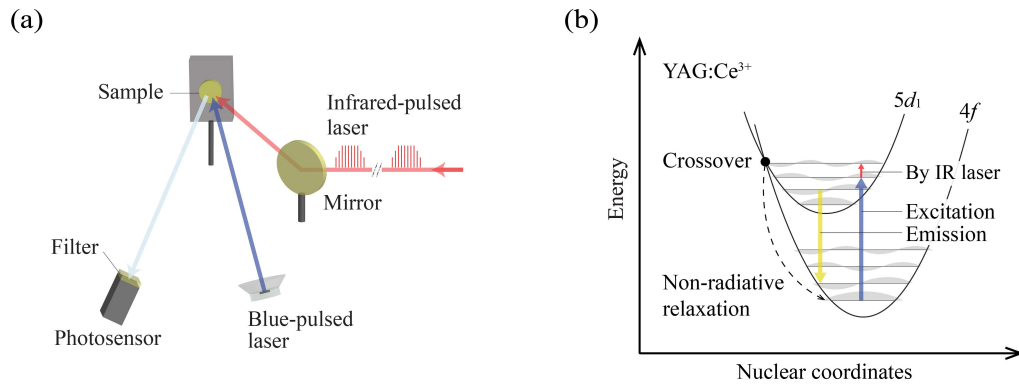


Figure 5.2: (a) Schematic setup for the two pulsed laser excitation experiment as described in Paper III, and (b) the luminescence quenching through $4f-5d$ crossover in $YAG:Ce^{3+}$.

Chapter 6

Conclusions and outlook

To conclude, this thesis has established the relationship between local structure, vibrational dynamics, and optical properties, such as emission wavelength and thermal quenching, in the technologically very important phosphor YAG:Ce³⁺. Our results have shown that the red-shifting effect of the emission spectra upon elevating temperature can be attributed to the activation of high-frequency phonons, related to symmetric stretching and symmetric bending motions of the CeO₈ moieties, which induce dynamical tetragonal distortions that strongly affect the optical properties of YAG:Ce³⁺. Specifically, the pronounced tetragonal distortions with increasing temperature leads to a red-shift of the emitted light. However, the emission turns to be blue shifted as the temperature increases above the Debye temperature as an effect of that thermal lattice expansion becomes predominant and weakens the tetragonal distortions at high temperatures. Moreover, it has been shown that three of the highest-frequency IR-active vibrational modes at 698, 724, and 789 cm⁻¹, are coupled with the excited electrons of the Ce³⁺ ions. This interaction between phonons and electrons induces non-radiative relaxation through 4*f*-5*d* crossover, thus, leading to thermal quenching. However, the pronounced reduction in emission intensity at elevated temperature is also found to be the result of thermal ionization. The co-existence of the two quenching mechanisms, electron-phonon coupling and thermal ionization, is qualitatively investigated, and both mechanisms are dependent on temperature in an Arrhenius manner. Based on their activation energies (0.24 and 0.38 eV for electron-phonon coupling and thermal ionization, respectively), electron-phonon coupling is shown to be more dominant than thermal ionization at low temperatures, and *vice versa*. Finally, a complete phonon assignment of the YAG crystal, based on symmetry coordinates, has been provided. Generally, the YAG phonon assignment is applicable to other garnets with the same site occupancy.

With a view to the future, I will investigate other oxide garnet phosphors, particularly Ce^{3+} -doped $\text{Y}_3\text{Al}_{5-x}\text{Ga}_x\text{O}_{12}$ ($\text{YAGG}:\text{Ce}^{3+}$), which show pronounced effects on the emission efficiency upon increasing Ga substitution. This leaves an intriguing question about the interplay between the structural variation caused by the Ga substitution and different quenching mechanisms, which will be further investigated based on our work at FELIX. Moreover, we will investigate the difference (if any) in the structure of the electronic ground and excited states in $\text{YAG}:\text{Ce}^{3+}$, by combining time-resolved optical excitation with time-resolved X-ray diffraction at the new beamline called FemtoMAX at the MAX IV laboratory in Lund, Sweden.

Acknowledgments

I would like to thank my supervisor, Maths, for all supports and giving me the opportunity to learn how to conduct research and collaborate with others. I am very grateful to Marco for his kind and inspiring supervision, and to Ezio for his always nice response to my questions and tremendous supports in the lab. I want to thank Paul for his knowledge input and inspiring discussions. Thanks to Suchinder for his motivating advice. Many thanks to Laura, Carin, Daria, Manfred, and Andrea for all the way cheering up. I am very grateful to every KMF friend and colleague for any kind of helps. Finally, I want to give my greatest appreciation to my parents, my sisters, my daughters (HuHu and AFu), and my dear wife (Feng-I) for endless supports.

Yuan-Chih

Bibliography

- [1] Siddha Pimputkar, James S Speck, Steven P DenBaars, and Shuji Nakamura. Prospects for LED lighting. *Nature Photonics*, 3(4):180–182, 2009.
- [2] European Commission. Green Paper - Lighting the Future: Accelerating the deployment of innovative lighting technologies. *Green Paper - Lighting the Future: Accelerating the deployment of innovative lighting technologies*, pages 1–19, 2011.
- [3] Shuji Nakamura, Takashi Mukai, and Masayuki Senoh. Candela-class high-brightness InGaN/AlGaIn double-heterostructure blue-light-emitting diodes. *Applied Physics Letters*, 64(13):1687–1689, 1994.
- [4] Isamu Akasaki, Hiroshi Amano, and Shuji Nakamura. Blue LEDs—Filling the world with new light. *Nobel Prize Lecture. Stockholm: The Nobel Foundation. Available at http://www.nobelprize.org/nobel_prizes/physics/laureates/2014/popular-physicsprize2014.pdf (accessed 13 February 2015)*, 2014.
- [5] Yuan-Chih Lin, Maths Karlsson, and Marco Bettinelli. Inorganic Phosphor Materials for Lighting. *Topics in Current Chemistry*, 374(2):1–47, 2016.
- [6] A Setlur. Phosphors for LED-based solid-state lighting. *The Electrochemical Society Interface*, 16(4):32, 2009.
- [7] S Ye, F Xiao, Y X Pan, Y Y Ma, and Q Y Zhang. Phosphors in phosphor-converted white light-emitting diodes: Recent advances in materials, techniques and properties. *Materials Science and Engineering: R: Reports*, 71(1):1–34, 2010.
- [8] Philippe F Smet, Anthony B Parmentier, and Dirk Poelman. Selecting conversion phosphors for white light-emitting diodes. *Journal of the electrochemical society*, 158(6):R37–R54, 2011.

- [9] Chun Che Lin and Ru-Shi Liu. Advances in Phosphors for Light-emitting Diodes. *The Journal of Physical Chemistry Letters*, 2(11):1268–1277, 2011.
- [10] Ali Kalaji, Paul J Saines, Nathan C George, and Anthony K Cheetham. Photoluminescence of cerium-doped $(\text{Ca}_{1-x}\text{Sr}_x)_3\text{RE}_2\text{Ge}_3\text{O}_{12}$ garnet phosphors for solid state lighting: Relating structure to emission. *Chemical Physics Letters*, 586:91–96, 2013.
- [11] G Blasse, B C Grabmaier, and B C Grabmaier. *Luminescent materials*, volume 44. Springer-Verlag Berlin, 1994.
- [12] Baldassare Di Bartolo. *Advances in nonradiative processes in solids*, volume 249. Springer Science & Business Media, 2013.
- [13] Chien-Chih Chiang, Ming-Shyong Tsai, and Min-Hsiung Hon. Luminescent Properties of Cerium-Activated Garnet Series Phosphor: Structure and Temperature Effects. *Journal of The Electrochemical Society*, 155(6):B517–B520, 2008.
- [14] Qiyue Shao, Yan Dong, Jianqing Jiang, Chao Liang, and Jinhua He. Temperature-dependent photoluminescence properties of $(\text{Y}, \text{Lu})_3\text{Al}_5\text{O}_{12}:\text{Ce}^{3+}$ phosphors for white LEDs applications. *Journal of Luminescence*, 131(5):1013–1015, 2011.
- [15] Yibo Chen, Menglian Gong, Gang Wang, and Qiang Su. High efficient and low color-temperature white light-emitting diodes with $\text{Tb}_3\text{Al}_5\text{O}_{12}:\text{Ce}^{3+}$ phosphor. *Applied Physics Letters*, 91(7):1117, 2007.
- [16] Yasuo Shimomura, Tetsuo Honma, Motoyuki Shigeiwa, Toshio Akai, Kaoru Okamoto, and Naoto Kijima. Photoluminescence and Crystal Structure of Green-Emitting $\text{Ca}_3\text{Sc}_2\text{Si}_3\text{O}_{12}:\text{Ce}^{3+}$ Phosphor for White Light Emitting Diodes. *Journal of The Electrochemical Society*, 154(1):J35–J38, 2007.
- [17] Arturas Katelnikovas, Tomas Bareika, Pranciškus Vitta, Thomas Jüstel, Holger Winkler, Aivaras Kareiva, Artras Žukauskas, and Gintautas Tamulaitis. $\text{Y}_{3-x}\text{Mg}_2\text{AlSi}_2\text{O}_{12}$: phosphors prospective for warm-white light emitting diodes. *Optical Materials*, 32(9):1261–1265, 2010.
- [18] Yi Luo and Zhiguo Xia. Effect of Al/Ga Substitution on Photoluminescence and Phosphorescence Properties of Garnet-Type $\text{Y}_3\text{Sc}_2\text{Ga}_{3-x}\text{Al}_x\text{O}_{12}:\text{Ce}^{3+}$ Phosphor. *The Journal of Physical Chemistry C*, 118(40):23297–23305, 2014.

- [19] Xinghong Gong, Jianhua Huang, Yujin Chen, Yanfu Lin, Zundu Luo, and Yidong Huang. Novel Garnet-Structure $\text{Ca}_2\text{GdZr}_2(\text{AlO}_4)_3\text{:Ce}^{3+}$ Phosphor and Its Structural Tuning of Optical Properties. *Inorganic Chemistry*, 53(13):6607–6614, 2014.
- [20] Anant A. Setlur, William J. Heward, Yan Gao, Alok M. Srivastava, R. Gopi Chandran, and Madras V. Shankar. Crystal Chemistry and Luminescence of Ce^{3+} -Doped $\text{Lu}_2\text{CaMg}_2(\text{Si,Ge})_3\text{O}_{12}$ and Its Use in LED Based Lighting. *Chemistry of Materials*, 18(14):3314–3322, 2006.
- [21] S Geller. Crystal chemistry of the garnets. *Zeitschrift für Kristallographie - Crystalline Materials*, 125(1-6):1–47, 1967.
- [22] Nathan C George, Andrew J Pell, Géraldine Dantelle, Katharine Page, Anna Llobet, M Balasubramanian, Guido Pintacuda, Bradley F Chmelka, and Ram Seshadri. Local Environments of Dilute Activator Ions in the Solid-State Lighting Phosphor $\text{Y}_{3-x}\text{Ce}_x\text{Al}_5\text{O}_{12}$. *Chemistry of Materials*, 25(20):3979–3995, 2013.
- [23] Paolo Ghigna, Sonia Pin, Cees Ronda, Adolfo Speghini, Fabio Piccinelli, and Marco Bettinelli. Local structure of the Ce^{3+} ion in the yellow emitting phosphor YAG:Ce. *Optical Materials*, 34(1):19–22, 2011.
- [24] Lars Vegard. Die konstitution der mischkristalle und die raumfüllung der atome. *Zeitschrift für Physik A Hadrons and Nuclei*, 5(1):17–26, 1921.
- [25] T Y Tien, E F Gibbons, R G DeLosh, P J Zacmanidis, D E Smith, and H L Stadler. Ce^{3+} Activated $\text{Y}_3\text{Al}_5\text{O}_{12}$ and Some of Its Solid Solutions. *Journal of The Electrochemical Society*, 120(2):278–281, 1973.
- [26] Pieter Dorenbos. Electronic structure and optical properties of the lanthanide activated $\text{RE}_3(\text{Al}_{1-x}\text{Ga}_x)_5\text{O}_{12}$ (RE=Gd, Y, Lu) garnet compounds. *Journal of Luminescence*, 134:310–318, 2013.
- [27] Nathan C George, Kristin A Denault, and Ram Seshadri. Phosphors for Solid-State White Lighting. *Annual Review of Materials Research*, 43(1):481–501, 2013.
- [28] Gary L Miessler and Donald A Tarr. Inorganic Chemistry. Pearson Education. *Upper Saddle River, NJ*, page 345, 2004.
- [29] G F Herrmann, J J Pearson, K A Wickersheim, and R A Buchanan. Crystal Field Effects for Ce^{3+} and Yb^{3+} in the Garnets. *Journal of Applied Physics*, 37(3):1312–1313, 1966.

- [30] Philip D Rack and Paul H Holloway. The structure, device physics, and material properties of thin film electroluminescent displays. *Materials Science and Engineering: R: Reports*, 21(4):171–219, 1998.
- [31] E G Rogers and P Dorenbos. A comparison of the transition metal 3d1 crystal field splitting with the lanthanide 5d1 crystal field splitting in compounds. *Journal of Luminescence*, 155:135–140, 2014.
- [32] Brian Henderson and G Frank Imbusch. *Optical spectroscopy of inorganic solids*, volume 44. Oxford University Press, 2006.
- [33] Volker Bachmann, Cees Ronda, and Andries Meijerink. Temperature quenching of yellow Ce^{3+} luminescence in YAG:Ce. *Chemistry of Materials*, 21(10):2077–2084, 2009.
- [34] K V Ivanovskikh, J M Ogiegłó, A Zych, C R Ronda, and A Meijerink. Luminescence Temperature Quenching for Ce^{3+} and Pr^{3+} d-f Emission in YAG and LuAG. *ECS Journal of Solid State Science and Technology*, 2(2):R3148–R3152, 2013.
- [35] D J Robbins. The Effects of Crystal Field and Temperature on the Photoluminescence Excitation Efficiency of Ce^{3+} in YAG. *Journal of The Electrochemical Society*, 126(9):1550–1555, 1979.
- [36] Jennifer L Wu, Gautam Gundiah, and A K Cheetham. Structure-property correlations in Ce-doped garnet phosphors for use in solid state lighting. *Chemical Physics Letters*, 441(46):250–254, 2007.
- [37] Ana Belén Muñoz-García and Luis Seijo. Structural, electronic, and spectroscopic effects of Ga codoping on Ce-doped yttrium aluminum garnet: First-principles study. *Phys. Rev. B*, 82(18):184118, nov 2010.
- [38] Joanna M Ogiegłó, Arturas Katelnikovas, Aleksander Zych, Thomas Justel, Andries Meijerink, and Cees R Ronda. Luminescence and luminescence quenching in $\text{Gd}_3(\text{Ga}, \text{Al})_5\text{O}_{12}$ scintillators doped with Ce^{3+} . *The Journal of Physical Chemistry A*, 117(12):2479–2484, 2013.
- [39] Yasushi Kanke and Alexandra Navrotsky. A Calorimetric Study of the Lanthanide Aluminum Oxides and the Lanthanide Gallium Oxides: Stability of the Perovskites and the Garnets. *Journal of Solid State Chemistry*, 141(2):424–436, 1998.
- [40] Luis Seijo and Zoila Barandiaran. Host effects on the optically active 4f and 5d levels of Ce^{3+} in garnets. *Phys. Chem. Chem. Phys.*, 15(44):19221–19231, 2013.

- [41] Luis Seijo and Zoila Barandiarán. 4f and 5d Levels of Ce^{3+} in D_2 8-fold oxygen coordination. *Optical Materials*, 35(11):1932–1940, 2013.
- [42] J P Hurrell, S P S Porto, I F Chang, S S Mitra, and R P Bauman. Optical Phonons of Yttrium Aluminum Garnet. *Phys. Rev.*, 173(3):851–856, sep 1968.
- [43] W G Fateley, Neil T McDevitt, and Freeman F Bentley. Infrared and Raman Selection Rules for Lattice Vibrations: The Correlation Method. *Appl. Spectrosc.*, 25(2):155–173, mar 1971.
- [44] Kazuo Nakamoto. *Infrared and Raman Spectra of Inorganic and Coordination Compounds, Theory and Applications in Inorganic Chemistry*. John Wiley & Sons, 2008.
- [45] R K Moore, W B White, and T V Long. Vibrational spectra of the common silicates: I. The garnets. *American Mineralogist*, 56(1-2):54, 1971.
- [46] A M Hofmeister and K R Campbell. Infrared spectroscopy of yttrium aluminum, yttrium gallium, and yttrium iron garnets. *Journal of Applied Physics*, 72(2):638–646, 1992.
- [47] K Papagelis, G Kanellis, S Ves, and G A Kourouklis. Lattice Dynamical Properties of the Rare Earth Aluminum Garnets ($RE_3Al_5O_{12}$). *physica status solidi (b)*, 233(1):134–150, 2002.
- [48] K Papagelis and S Ves. Vibrational properties of the rare earth aluminum garnets. *Journal of Applied Physics*, 94(10):6491–6498, 2003.
- [49] Charles W Struck and William H Fonger. *Understanding luminescence spectra and efficiency using Wp and related functions*, volume 13. Springer Science & Business Media, 2012.
- [50] G Blasse. Thermal quenching of characteristic fluorescence. *The Journal of Chemical Physics*, 51(8):3529–3530, 1969.
- [51] Kun Huang and Avril Rhys. Theory of Light Absorption and Non-Radiative Transitions in F-Centres. *Proceedings of the Royal Society of London A: Mathematical, Physical and Engineering Sciences*, 204(1078):406–423, 1950.

- [52] Mathijs de Jong, Luis Seijo, Andries Meijerink, and Freddy T Rabouw. Resolving the ambiguity in the relation between Stokes shift and Huang–Rhys parameter. *Physical Chemistry Chemical Physics*, 17(26):16959–16969, 2015.
- [53] C W Struck and W H Fonger. Unified model of the temperature quenching of narrow-line and broad-band emissions. *Journal of Luminescence*, 10(1):1–30, 1975.
- [54] Cornelis R Ronda. *Luminescence: from theory to applications*. John Wiley & Sons, 2007.
- [55] Ana Belén Muñoz-García, Zoila Barandiarán, and Luis Seijo. Anti-site defects in Ce-doped YAG ($\text{Y}_3\text{Al}_5\text{O}_{12}$): first-principles study on structures and 4f–5d transitions. *Journal of Materials Chemistry*, 22(37):19888–19897, 2012.
- [56] C R Stanek, K J McClellan, M R Levy, C Milanese, and R W Grimes. The effect of intrinsic defects on $\text{RE}_3\text{Al}_5\text{O}_{12}$ garnet scintillator performance. *Nuclear Instruments and Methods in Physics Research Section A: Accelerators, Spectrometers, Detectors and Associated Equipment*, 579(1):27–30, 2007.
- [57] Jumpei Ueda, Setsuhisa Tanabe, and Takayuki Nakanishi. Analysis of Ce^{3+} luminescence quenching in solid solutions between $\text{Y}_3\text{Al}_5\text{O}_{12}$ and $\text{Y}_3\text{Ga}_5\text{O}_{12}$ by temperature dependence of photoconductivity measurement. *Journal of applied physics*, 110(5):53102, 2011.
- [58] E der Kolk, S A Basun, G F Imbusch, and W M Yen. Temperature dependent spectroscopic studies of the electron delocalization dynamics of excited Ce ions in the wide band gap insulator, Lu_2SiO_5 . *Applied Physics Letters*, 83 (9), 2003, 2003.
- [59] Jumpei Ueda, Pieter Dorenbos, Adrie J J Bos, Andries Meijerink, and Setsuhisa Tanabe. Insight into the thermal quenching mechanism for $\text{Y}_3\text{Al}_5\text{O}_{12}:\text{Ce}^{3+}$ through thermoluminescence excitation spectroscopy. *The Journal of Physical Chemistry C*, 119(44):25003–25008, 2015.
- [60] Stephen W Allison, J R Buczyrna, R A Hansel, D G Walker, and G T Gillies. Temperature-dependent fluorescence decay lifetimes of the phosphor $\text{Y}_3(\text{Al}_{0.5}\text{Ga}_{0.5})_5\text{O}_{12}:\text{Ce}$ 1%. *Journal of Applied Physics*, 105(3):36105, 2009.

- [61] Rachael A Hansel, S W Allison, and D G Walker. Temperature-dependent luminescence of Ce^{3+} in gallium-substituted garnets. *Applied Physics Letters*, 95(11):114102, 2009.
- [62] Daniel C Harris and Michael D Bertolucci. *Symmetry and spectroscopy: an introduction to vibrational and electronic spectroscopy*. Courier Corporation, 1978.
- [63] Norman Sheppard. *The historical development of experimental techniques in vibrational spectroscopy*. Wiley Online Library, 2002.
- [64] Gordon Leslie Squires. *Introduction to the theory of thermal neutron scattering*. Cambridge university press, 2012.
- [65] Roger Pynn. Neutron scattering: a primer. *Los Alamos Science*, 19:1–31, 1990.
- [66] Philip C H Mitchell, Stewart F Parker, Anibal J Ramirez-Cuesta, and John Tomkinson. *Vibrational spectroscopy with neutrons: with applications in chemistry, biology, materials science and catalysis*, volume 3. World Scientific, 2005.
- [67] ILL :: Neutrons for science : Inelastic neutron scattering. Available at <https://www.ill.eu/science-technology/science-at-ill/why-and-how/neutron-techniques/inelastic-neutron-scattering/> (accessed 7 September 2016).
- [68] Carl W F T Pistorius. The Harmonic Vibration Problem of the Cubic XY_8 Molecule. *Bulletin des Sociétés Chimiques Belges*, 68(10-12):630–642, 1959.
- [69] Richard Conger Powell. *Symmetry, group theory, and the physical properties of crystals*, volume 824. Springer, 2010.
- [70] Jose Solé, Luisa Bausa, and Daniel Jaque. *An introduction to the optical spectroscopy of inorganic solids*. John Wiley & Sons, 2005.
- [71] A J J Bos. Theory of thermoluminescence. *Radiation Measurements*, 41, Supple:S45 – S56, 2006.
- [72] FEL operating principle - FELIX Laboratory. Available at <http://www.ru.nl/felix/about-felix/about-felix/fel-operating-principle/> (accessed 28 September 2016).

- [73] Eric B Szarmes. Classical Theory of Free-Electron Lasers. *Classical Theory of Free-Electron Lasers*, 2014.
- [74] Henry P Freund. *Principles of free-electron lasers*. Springer Science & Business Media, 2012.
- [75] Brian C Smith. *Fundamentals of Fourier transform infrared spectroscopy*. CRC press, 2011.
- [76] Bernhard Schrader. *Infrared and Raman spectroscopy: methods and applications*. John Wiley & Sons, 2008.
- [77] S F Parker, J Tomkinson, A J Ramirez-Cuesta, and D Colognesi. The Tosca user-guide. Technical report, Council for the Central Laboratory of the Research Councils (United Kingdom), 2003.
- [78] USB2000+ (Custom) - Ocean Optics. Available at <http://oceanoptics.com/wp-content/uploads/USB2000-Operating-Instructions1.pdf> (accessed 29 September 2016).
- [79] D Oepts, A F G der Meer, and P W Van Amersfoort. The free-electron-laser user facility FELIX. *Infrared physics & technology*, 36(1):297–308, 1995.
- [80] FELIX in more detail - FELIX Laboratory. Available at <http://www.ru.nl/felix/about-felix/about-felix/felix-laboratory/> (accessed 7 September 2016).